

# Dynamics of large-scale circulation of turbulent thermal convection in a horizontal cylinder

Hao Song<sup>1</sup>, Eric Brown<sup>2</sup>, Russell Hawkins<sup>3</sup> and Penger Tong<sup>1,†</sup>

<sup>1</sup>Department of Physics, Hong Kong University of Science and Technology, Clear Water Bay, Kowloon, Hong Kong

<sup>2</sup>Department of Mechanical Engineering and Materials Science, Yale University, New Haven, CT 06520, USA

<sup>3</sup>School of Natural Sciences, University of California, Merced, CA 95343, USA

(Received 3 May 2013; revised 8 November 2013; accepted 5 December 2013;  
first published online 6 January 2014)

A systematic study of the effects of cell geometry on the dynamics of large-scale flows in turbulent thermal convection is carried out in horizontal cylindrical cells of different lengths filled with water. Four different flow modes are identified with increasing aspect ratio  $\Gamma$ . For small aspect ratios ( $\Gamma < 0.16$ ), the flow is highly confined in a thin disc-like cell with a quasi-two-dimensional (quasi-2D) large-scale circulation (LSC) in the circular plane of the cell. For larger aspect ratios ( $\Gamma > 0.16$ ), we observe periodic switching of the angular orientation of the rotation plane of LSC between the two longest diagonals of the cell. The sides of the container along which the LSC oscillates changes at a critical aspect ratio  $\Gamma_c = 0.82$ . The measured switching period is equal to the LSC turnover time for  $\Gamma < \Gamma_c$ , shows a sharp increase at  $\Gamma_c$  and decays exponentially to the LSC turnover time with increasing  $\Gamma$ . For  $\Gamma > 1.3$ , a periodic rocking of LSC along the long axis of the cylinder is also observed. The measured probability density function  $P(\theta)$  of the LSC orientation  $\theta$  peaks at the two diagonal positions, and its shape is described by a phenomenological model proposed by Brown & Ahlers (*Phys. Fluids*, vol. 20, 2008*b*, 075101; *J. Fluid Mech.*, vol. 638, 2009, pp. 383–400). Using this model, we describe the dynamics of the LSC orientation  $\theta$  by stochastic motion in a double-well potential. The potential is predicted from a model in which the sidewall shape produces an orientation-dependent pressure on the LSC. This model also captures key features of the four flow modes. The experiment reveals an interesting array of rich dynamics of LSC in the horizontal cylinders, which are very different from those observed in the upright cylindrical convection cells. The success of the model for both upright and horizontal cylinders suggests that it can be applied to different geometries.

**Key words:** low-dimensional models, turbulent convection, turbulent transition

---

## 1. Introduction

Turbulent thermal convection, where warm fluid rises and cold fluid falls and their mixing produces convective turbulence, is ubiquitous in nature and technology. It is found in the Earth's mantle and outer core, in the atmosphere and oceans, and in

†Email address for correspondence: [penger@ust.hk](mailto:penger@ust.hk)

the outer layer of the Sun (Ahlers, Grossmann & Lohse 2009b). In the laboratory, one conducts controlled thermal convection experiments by using a Rayleigh–Bénard convection (RBC) cell, where a fluid layer of height  $H$  and lateral dimension  $D$  is heated from below and cooled from the top so that heat is transferred vertically from the lower warm surface to the upper cold surface. When the temperature difference  $T$  across the fluid layer is large enough, the bulk fluid becomes turbulent and heat is transported predominantly by convection (Kadanoff 2001; Ahlers *et al.* 2009b). Up to now, many of the turbulent convection experiments were conducted in small upright cylindrical cells with the cylinder diameter  $D$  being comparable to its height  $H$ . These experiments have resulted in a large body of knowledge about the scaling of global heat transport (Castaing *et al.* 1989; Cioni, Ciliberto & Sommeria 1997; Niemela *et al.* 2000; Chavanne *et al.* 2001; Funfschilling *et al.* 2005; Sun *et al.* 2005a; Urban, Musilová & Skrbek 2011), structure (Qiu & Tong 2001a; Sun, Xia & Tong 2005b) and oscillations (Qiu & Tong 2001b; Brown & Ahlers 2009; Zhou *et al.* 2009) of the large-scale circulation (LSC), the dynamics of viscous and thermal boundary layers (Belmonte, Tilgner & Libchaber 1993; Xin, Xia & Tong 1996; Sun, Cheung & Xia 2008; du Puits, Resagk & Thess 2009) and the statistical properties of local temperature (Castaing *et al.* 1989; Du & Tong 2001; Sun, Zhou & Xia 2006) and velocity (Qiu *et al.* 2004) fluctuations. Our current theoretical understanding of convective turbulence is largely built upon this body of experimental results (Ahlers *et al.* 2009b; Lohse & Xia 2010).

While the use of small-aspect-ratio ( $\Gamma = D/H$ ) cylinders has the advantages of simple cell geometry, better experimental control and relatively large Rayleigh numbers ( $Ra$ ) attainable for a given cell diameter, a natural question regarding this system is: To what extent can the experimental results and theoretical predictions for small-aspect-ratio cells be applied to laterally large systems? This is an important question because one wants to understand which aspects of convection are universal and which depend on the details of spatial geometry (Daya & Ecke 2001). Such an understanding is needed for a large number of practical problems, ranging from the thermal convection processes in buildings (Hunt & Linden 1999) and metal production (Brent, Voller & Reid 1988) to natural convection occurring in the atmosphere (Hartmann, Moy & Fu 2001) and oceans (Marshall & Schott 1999) and at geophysical and astrophysical scales, such as convection in the Earth's mantle (McKenzie, Roberts & Weiss 1974) and stars (Cattaneo, Emonet & Weiss 2003).

Experimental efforts have been made recently to understand the sidewall effect. The experiments carried out in Göttingen (He *et al.* 2012), Hong Kong (Sun *et al.* 2005a) and Ilmenau (du Puits, Resagk & Thess 2007) using large upright cylindrical cells with diameter larger than 1 m studied the scaling laws of the global heat transport and dynamics of the LSC, which spans the entire convection cell. The dynamics of LSC, such as the torsional mode (Funfschilling & Ahlers 2004), rotations with cessation (Brown & Ahlers 2006; Xi, Zhou & Xia 2006), random reversals (Xi & Xia 2007) and the sloshing mode (Brown & Ahlers 2009; Xi *et al.* 2009) were reported in recent years. More recently, Song and Tong carried out a systematic study of scaling laws in turbulent RBC under different geometry (Song & Tong 2010). Instead of using a large upright cylinder, a new convection cell of smaller size but with different geometry was constructed. The new cell has a shape of horizontal cylinder, as shown in figure 1. The top and bottom 1/3 of the circular sidewall of the cylinder are made of copper to provide constant cooling and heating, respectively. Sandwiched in the middle of the circular sidewall are two pieces of thermal insulating (curved) plate made of Plexiglas. L. P. Kadanoff (Private communication with P. Tong, 2000)

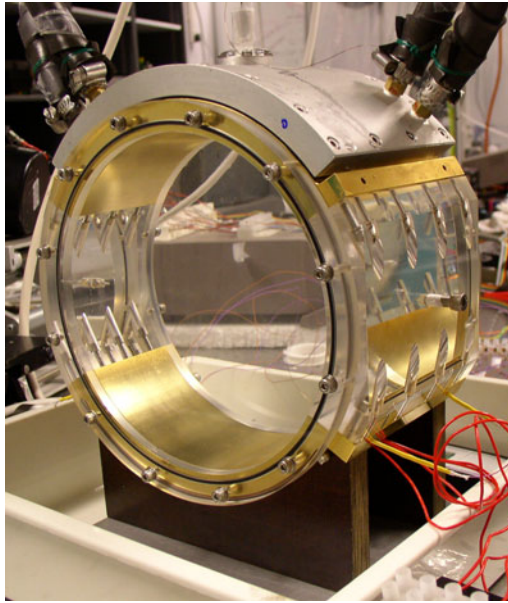


FIGURE 1. (Colour online) Assembly of a horizontal cylindrical convection cell with aspect ratio  $\Gamma = 0.5$ . The top and bottom 1/3 of the circular sidewall of the cylinder are made of copper to provide constant cooling and heating, respectively. Sandwiched in the middle of the circular sidewall are two pieces of thermal insulating (curved) plate made of Plexiglas.

first proposed to build such a kind of cell in the hope that the circular cross-section of the horizontal cylinder could better accommodate the LSC. The experiment revealed that the measured Nusselt number  $Nu(Ra)$ , which is a normalized total heat flux, and the Reynolds number  $Re(Ra)$  associated with the LSC are insensitive to the change of cell geometry; their scaling over varying Rayleigh numbers  $Ra$  remains unchanged. Evidently, the boundary-layer dynamics, which determine the global heat transport, and the buoyancy forces which drive the large-scale flow remain the same under different cell geometry. Despite this universality, the LSC dynamics are known to change with the boundary shape, as the observations in upright cylindrical cells (Brown & Ahlers 2006; Xi *et al.* 2006), rectangular cells (Zhou, Sun & Xia 2007), and thin circular cells (Song & Tong 2010) differ. If one wants to understand which aspects of convection are universal, it is important to ask which aspects of the LSC dynamics change with the boundary shape, and can these changes be predicted? So far, there have been no systematic studies of how the LSC changes with boundary shape (Chillà & Schumacher 2012).

In this paper, we report an experimental study of the dynamics of the LSC in the horizontal cylinder filled with water. We carry out systematic temperature, velocity and flow visualization measurements to fully characterize the structural changes of the LSC with varying aspect ratios  $\Gamma$ . The experiment reveals an interesting array of rich dynamics of the LSC in the horizontal cylinder, which have not been observed in the upright cylinders. With increasing values of  $\Gamma$ , the LSC develops from a quasi-two-dimensional (quasi-2D) circulation ( $\Gamma = 0.16$ ) to a three-dimensional (3D) coherent structure. For all of the cells with  $0.1 < \Gamma < 1.69$ , a well-defined oscillation is observed in the temperature, velocity and flow visualization

measurements. Oscillations in the quasi-2D flow are found to be caused by the periodic eruption of thermal plumes from the boundary layers. This effect can be explained by Villermaux's model involving two coupled nonlinear dynamic equations for the instabilities of the upper and lower thermal boundary layers (Villermaux 1995; Song, Villermaux & Tong 2011). Oscillations in the 3D flow result from the periodic switching of the LSC orientation between the two diagonals of the horizontal cylinder. This diagonal switching has two phases. For  $0.16 < \Gamma < 0.82$ , the oscillation period  $t_0$  is found to be approximately equal to the LSC turnover time  $t_t$  (the time taken for the LSC to go around for one cycle). For  $\Gamma > 0.82$ , the normalized oscillation period  $t_0/t_t$  takes a sharp jump to a value of 5.3 and then exponentially decays to unity with increasing  $\Gamma$ . The measured probability density function (p.d.f.)  $P(\theta)$  of the angular position  $\theta(t)$  of the LSC orientation peaks at the two diagonal positions and its shape is adequately described by a model proposed by Brown & Ahlers (2008a,b). Using this model we describe the dynamics of the LSC orientation  $\theta(t)$  with stochastic motion in a double-well potential. This model captures key features of the observed flow modes.

The remainder of the paper is organized as follows. We first describe the experimental apparatus and methods in §2. Experimental results are reported in §3. Further theoretical analyses are provided in §4. Finally, the work is summarized in §5.

## 2. Experimental apparatus and methods

### 2.1. Horizontal convection cell

The convection experiment is conducted in four horizontal cylindrical cells with the same inner diameter  $D = 18.8$  cm but their horizontal length  $L$  is different. The four fixed lengths used are  $L = 31.8, 18.8, 9.4$  and  $3.0$  cm. The corresponding aspect ratio of the four cells is  $L/D = 1.69, 1.0, 0.5$  and  $0.16$ , respectively. Water is used as the convecting fluid. For all the four convection cells, the top and bottom 1/3 of the circular sidewall of the cylinder is made of copper with a wall thickness of 0.5 cm. The surface of the conducting plates is electroplated with a thin layer of gold. Sandwiched in the middle of the circular sidewall are two pieces of a thermal insulating (curved) plate made of transparent Plexiglas. The two flat end walls of the cell are made of the same Plexiglas with a wall thickness of 2.3 cm.

Except for the difference in cell shape, the other aspects of the apparatus and the experimental procedures used for the horizontal cylinder are similar to those used for the upright cylinder, which have been described elsewhere (Du & Tong 2000; Qiu *et al.* 2004). Two silicon rubber film heaters connected in parallel are sandwiched on the back side of the bottom 1/3 conducting plate to provide constant and uniform heating. A dc power supply with 99.99 % long-term stability is used to provide the heating power. The voltage applied to the heaters varies from 15 to 85 V, and the corresponding heating power is in the range between 10 and 300 W. The top 1/3 conducting plate is in contact with a cooling chamber consisting of many squarely winded water channels of 1 cm in width. These water channels are doubly wound with a channel separation of 0.5 cm, so that the incoming cooler fluid and the outgoing warmer fluid in adjacent channels can compensate with each other and provide uniform cooling on the top plate. A temperature-controlled circulator (Neslab, RTE 740) with a temperature stability of 0.01 °C is used to circulate the cooling water and maintain the top-plate temperature.

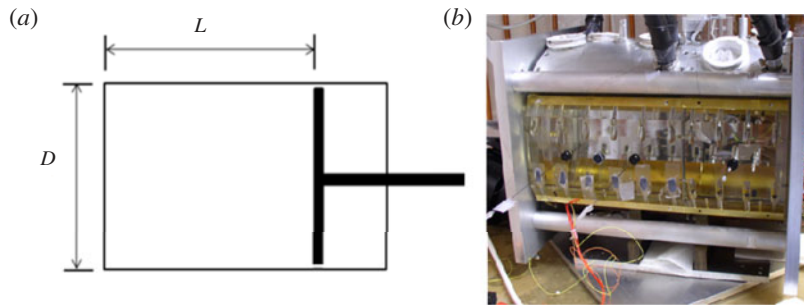


FIGURE 2. (Colour online) (a) Sketch of the  $\Gamma = 1.69$  horizontal cylindrical cell with a mobile piston installed so that the length  $L$  of the left flow chamber can be varied in the range of 0–30 cm. (b) Assembly of the  $\Gamma = 1.69$  horizontal cylindrical cell (without piston).

To have a horizontal flow chamber with a variable length  $L$ , we install a mobile piston in the  $\Gamma = 0.5$  and  $\Gamma = 1.69$  cells. The piston is made of a Plexiglas plate of thickness 1.0 cm and diameter 18.6 cm, which is 2 mm smaller than the diameter  $D$  of the cell, allowing the piston to move freely along the axis of the cylindrical cell. Figure 2(a) shows a sketch of the  $\Gamma = 1.69$  horizontal cylindrical cell with a mobile piston installed. The piston divides the cell into two flow chambers, which are connected by a narrow gap, so that the length  $L$  of the left flow chamber (without the handle of the piston) can be varied in the range of 0–30 cm. The aspect ratio of the left flow chamber,  $\Gamma = L/D$ , is thus in the range of 0–1.6 (the  $\Gamma = 0.5$  cell is used to cover the small  $\Gamma$  range). Figure 2(b) shows the assembly of the  $\Gamma = 1.69$  cell (without piston). This cell is made by combining two shorter cylindrical cells and an aluminium frame with two flat plates and four supporting posts is used to clamp the two separate cells together. For the measurements in the left flow chamber, the entire cell is filled with water and is heated (and cooled) uniformly across the whole conducting plate. It was reported recently that the coupling of an unsealed cell to the outside chamber can produce some peculiar effect on the measured Nusselt number  $Nu(Ra)$  at high Rayleigh numbers ( $Ra \sim 10^{14}$ ) (Ahlers, Funfschilling & Bodenschatz 2009a). To examine the coupling effect of the right flow chamber to the left flow chamber, we compare the flow patterns and the main characteristics of the temperature and velocity measurements carried out in the left flow chamber with those obtained in the horizontal cylinders with the same fixed aspect ratio ( $\Gamma = 1.0, 0.5$  and  $0.16$ ) but without the piston. Identical results are found in the two types of the flow cells, indicating that the coupling effect of the right flow chamber to the left flow chamber is negligibly small for the measurements presented in this paper, which are obtained at much lower values of  $Ra$  compared with the experiment mentioned above (Ahlers *et al.* 2009a).

The entire convection cell is placed inside a thermostat box, whose temperature matches the mean temperature of the bulk fluid, which is fixed at 30 °C. At this temperature, the Prandtl number  $Pr = \nu/\kappa$  is fixed at  $Pr = 5.4$ . Here  $\nu$  and  $\kappa$  are, respectively, the kinematic viscosity and thermal diffusivity of the convecting fluid. In the convection experiment, the control parameter is the Rayleigh number  $Ra$ , which is defined as  $Ra = g \Delta T D^3 / (\nu \kappa)$ , where  $g$  is the gravitational acceleration,  $\Delta T$  is the temperature difference across the fluid (i.e. between the top and bottom conducting plates) and  $\beta$  is the thermal expansion coefficient of the convecting fluid. Here the

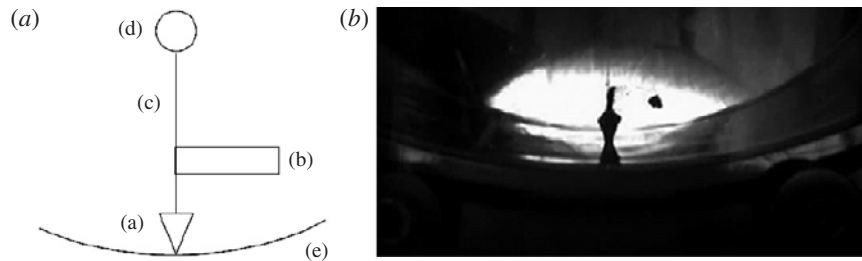


FIGURE 3. (a) Sketch of a free rotating floater used to indicate the direction of the large-scale flow: (a) cone shaped plummet, (b) rectangular flag, (c) connecting line, (d) buoyant styrofoam sphere and (e) lower conducting plate. (b) Image of an actual floater standing on the centre of the bottom conducting plate of the  $\Gamma = 1.69$  cell. The rectangular flag points to the direction of mean flow.

cylinder diameter  $D$  is used as the cell height. In the experiment to be discussed below, the value of  $Ra$  is varied in the range between  $10^8$  and  $10^{10}$ .

The temperature of each conducting plate is measured using four thermistors (Omega, Model 44006) of diameter 2.4 mm and time constant 1 s with an accuracy of 0.05 °C. These thermistors are embedded in the four corners of the conducting plate and are 5 mm away from the convecting fluid. A digital multimeter (Keithley 2700) is used to simultaneously measure the resistance value of these thermistors. In the experiment, the temperature difference  $\Delta T$  between the top and bottom plates varies from 1.5 to 35 °C depending on the heating power. By adjusting the temperature of the cooling water, we maintain the temperature of the bulk fluid at 30 °C for all of the measurements. The temperature stability of the top and bottom plates is found to be within 0.05 °C in standard deviation for low-power heating and within 0.15 °C for high-power heating. These temperature variations are less than 3.3 % of the minimum  $\Delta T$  used in the experiment.

## 2.2. Temperature, velocity and flow visualization measurements

The local temperature of the convecting fluid is measured using a waterproof thermistor (Thermometrics, AB6E3-B05) of diameter 0.3 mm and time constant 10 ms (in water). This thermistor is connected to an ac transformer bridge as a resistor arm and the other resistor arm is connected to a variable resistor to balance the bridge. The bridge is driven by a lock-in amplifier (Stanford, SR 830) at a working frequency  $f = 1$  kHz. The output signals are digitized by an analogue-to-digital card at the sampling rate of 40 Hz. All of the thermistors used to measure the local temperature of the convecting fluid are calibrated individually with an accuracy of 5 mK.

The local velocity is measured using a laser Doppler velocimetry (LDV) system (TSI Inc.) together with an argon-ion laser (Coherent Innova 90). Monodispersed polystyrene latex spheres of 5.1  $\mu\text{m}$  in diameter are used as seed particles. A shadowgraph technique (Settles 2001; Song 2011) is used to visualize the large-scale flow and thermal plumes in small-aspect-ratio cells. For large-aspect-ratio cells, a homemade floater is used to indicate the direction of the large-scale flow. It consists of a plummet (see (a) in figure 3a), which is made of tin and has an inverted cone shape of 5 mm in height. As shown in figure 3(a), the plummet has a sharp end tip in contact with the bottom plate of the cell (e) and its weight is balanced by a

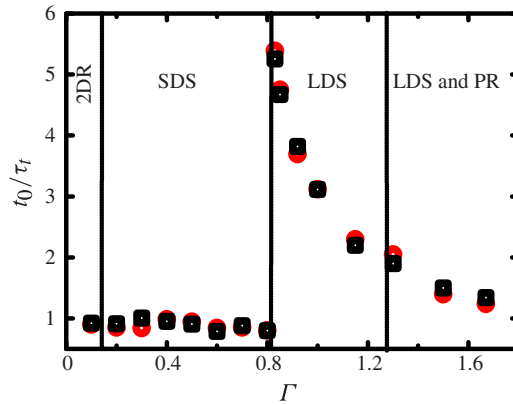


FIGURE 4. (Colour online) Normalized oscillation period  $t_0/\tau_t$  by the LSC turnover time  $\tau_t$  as a function of the aspect ratio  $\Gamma$ . The circles (shown in red online) are obtained at  $Ra = 2.7 \times 10^9$  and the squares (shown in black) are obtained at  $Ra = 5.5 \times 10^9$ .

buoyant styrofoam sphere of 5 mm in diameter (d). The styrofoam sphere is linked to the floater by a fishing line (c). The buoyant mass of the floater system is adjusted so that it can freely rotate when pushed by the mean flow but its position remains stationary in the flow. The floater is placed at the centre of the bottom plate, which is a symmetric point in the cell and always stays in the rotation plane of the LSC. A rectangular flag (15 mm  $\times$  3 mm) with a small piece of white plastic sheet attached to its end (see (b) in figure 3a) is attached to the floater system. This flag points to the direction of mean flow. Figure 3(b) shows the image of an actual floater standing on the bottom centre of the  $\Gamma = 1.69$  cell. A digital camera is used to take movies of the floater's motion at a sampling rate of 1 frame  $s^{-1}$ . These movies are used to find the angular position  $\theta$  of the flag using a homemade MATLAB program. Because the flag follows the flow well, its angular position  $\theta$  can be considered as the angular orientation of the LSC rotation plane.

### 3. Experimental results

#### 3.1. Dynamic phase diagram

The convective flow exhibits four different steady states (or dynamic phases) with increasing values of  $\Gamma$ . These flow modes are distinguished in the experiment by their unique flow patterns. For small aspect ratios ( $\Gamma < 0.16$ ), the flow is highly confined in a thin disc-like cell with a quasi-two-dimensional rotation (quasi-2DR) in the circular plane of the cell. For larger aspect ratios ( $\Gamma > 0.16$ ), the LSC orientation periodically switches between the two longest diagonals of the cell. For  $0.16 < \Gamma < 0.82$ , the LSC passes along the curved sidewall as it switches between diagonals, which we refer to as small-diagonal switching (SDS). For  $0.82 < \Gamma < 1.69$ , the LSC passes along the flat sidewall as it switches between diagonals, which we refer to as large-diagonal switching (LDS). For  $1.3 < \Gamma < 1.69$ , there is also a coexisting phase in which the LSC plane undergoes a periodic rocking (PR) around the long axis of the cylinder. Figure 4 shows the 'phase diagram' of the convection system. The vertical axis shows the measured switching period  $t_0/\tau_t$ , normalized by the large-scale turnover time  $\tau_t = D/V_h$ , as a function of  $\Gamma$ . Here  $V_h$  is the velocity component of the LSC along the circumference  $D$  of the horizontal cell. More details about the measurement of  $t_0/\tau_t$

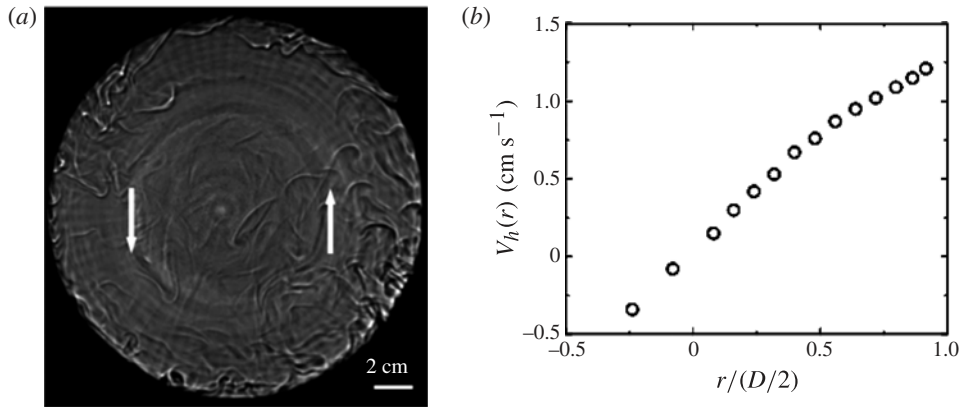


FIGURE 5. (a) A shadowgraph showing the large-scale flow and the spatial distribution of thermal plumes in the  $\Gamma = 0.16$  cell at  $Ra = 4 \times 10^9$ . (b) Measured horizontal velocity profile  $V_h(r)$  at  $Ra = 6 \times 10^9$ . The measurements are made along the vertical diameter of the cell from the cell centre ( $r=0$ ) to the centre of the bottom plate ( $r=D/2$ ).

are given in § 3.4. The circles (shown in red online) are obtained at  $Ra = 2.7 \times 10^9$  and the squares (shown in black) are obtained at  $Ra = 5.5 \times 10^9$ . It is seen that the normalized  $t_0/\tau$  does not change much with  $Ra$  (see more discussions on figure 12a below). We describe each of the flow modes in detail in the following subsections.

### 3.2. Two-dimensional rotation

Figure 5(a) shows the large-scale flow and the spatial distribution of thermal plumes in the  $\Gamma = 0.16$  cell. The arrows indicate the direction of the large-scale flow. It is found that the thermal plumes organize themselves with rising warm plumes (darker) on the right and falling cold plumes (brighter) on the left. The spatially separated warm and cold plumes exert buoyancy forces on the fluid and drive the vertical flow near the sidewall. The central region is sheared by the rising and falling plumes, resulting in a LSC confined in the circular plane of the cell. The fly-wheel-like flow structure is also observed in the measured horizontal velocity profile  $V_h(r)$  along the vertical diameter of the cell from the cell centre ( $r=0$ ) to the centre of the bottom plate ( $r=D/2$ ), as shown in figure 5(b). The velocity field in the circular plane of the cell has a zero mean at the centre and increases linearly with the radial distance  $r$  in the bulk region of the flow. A similar flow structure for the LSC was also observed in the  $\Gamma = 1$  upright cylinders (Qiu & Tong 2002).

Even in this confined space, where it is impossible to excite the torsional and sloshing flow modes (Funfschilling & Ahlers 2004; Brown & Ahlers 2009; Xi *et al.* 2009) in the horizontal directions, we observed a well-defined oscillation frequency in the power spectrum of five different signals, including local (fluid) temperature, local conducting plate temperature, local horizontal velocity, time-varying total heat flux of the top conducting plate and image intensity variations. In a recent letter (Song *et al.* 2011), we have reported the experimental study of the physical origin of the coherent oscillations in the 2DR state. The experiment demonstrated that the coherent oscillations are produced by the periodic emission of thermal plumes from the boundary layers, which gives rise to periodic pulses of forcing, resulting in a pulsed LSC in the thin cell. The experimental results were explained by a new solution of Villiermaux's model involving two coupled nonlinear delayed equations for

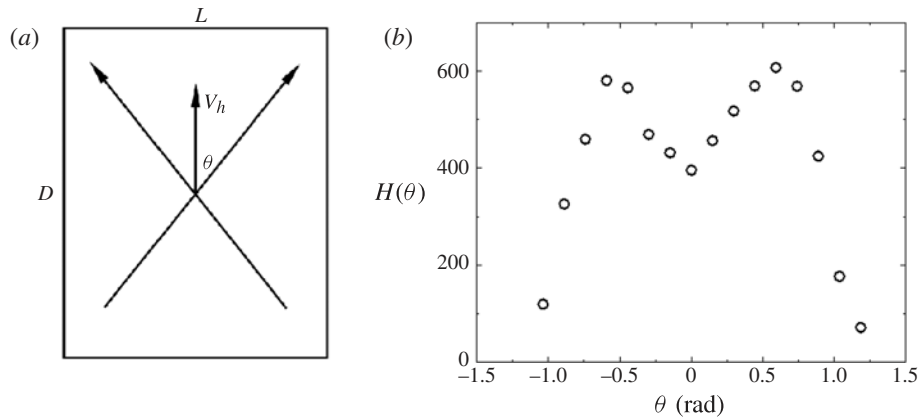


FIGURE 6. (a) Angular position of the rotation plane of the LSC in the SDS phase (top view). The arrows indicate the two diagonal orientations of the LSC in the SDS phase. The rectangular box depicts the cross-sectional area at the middle height of the horizontal cylinder with  $L$  being the length of the cell and  $D$  being its diameter. (b) Measured histogram  $H(\theta)$  of the LSC orientation in the  $\Gamma = 0.7$  cell at  $Ra = 5.5 \times 10^9$ .

the instabilities of the upper and lower thermal boundary layers (Villermaux 1995; Song *et al.* 2011).

### 3.3. Small- $\Gamma$ diagonal switching

As  $\Gamma$  increases, the LSC is no longer confined within the circular plane of the cell and a 3D LSC develops. It is found that the rotation plane of the LSC prefers to stay along the two diagonals of the cell. Using a small homemade floater, we obtain the time series data of the angular position  $\theta(t)$  of the LSC orientation. The definition of  $\theta$  is depicted in figure 6(a). Figure 6(b) shows the histogram  $H(\theta)$  of the LSC orientation in the  $\Gamma = 0.7$  cell. The obtained  $H(\theta)$  peaks at two angular positions  $\theta_0 \pm 0.6$ , indicating that they are the two most probable angular positions for the LSC orientation. The two peak positions of the measured  $H(\theta)$  coincide with the angular position of the two diagonals of the  $\Gamma = 0.7$  cell:  $\theta = \pm \arctan(\Gamma = 0.7) = \pm 0.61$ . From the time series data  $\theta(t)$ , we also calculate the auto-correlation function of the LSC orientation  $\theta(t)$ ,

$$C(\tau) = \langle \theta(t) \theta(t + \tau) \rangle / \sigma^2, \quad (3.1)$$

where  $\sigma$  is the root-mean-square (r.m.s.) value of  $\theta(t)$ . The oscillatory behaviour of the measured  $C(\tau)$ , as shown in figure 7, suggests that the LSC orientation oscillates periodically between the two diagonals of the cell. The oscillation period  $t_0$  ( $\approx 25$  s) can be determined from the temporal distance between two adjacent peaks in  $C(\tau)$ . Figures 6 and 7 thus demonstrate that the rotation plane of the LSC in the SDS phase switches periodically from one diagonal of the cell to the other.

The floater system works well for high- $Ra$  flows, which are strong enough to drive the rotation of the floater. For low- $Ra$  flows ( $Ra \approx 10^8$ ), however, the flow is too weak to force the floater to rotate. To increase the dynamic range of the experiment, we use the LDV setup to measure the horizontal velocity  $V_h(t)$  at a location 1 cm above the centre of the bottom conducting plate. This is a symmetric location of the cell, which always stays in the LSC rotation plane regardless of its orientation. As shown in figure 6(a), the measured  $V_h(t)$  is a projection of the LSC velocity along the  $\theta = 0$  direction. Figure 8(b) shows the time series data of the measured  $V_h(t)$  in

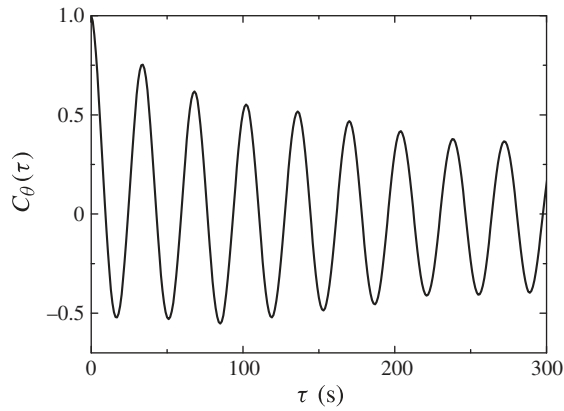


FIGURE 7. Measured auto-correlation function  $C_\theta(\tau)$  of the angular position of the LSC orientation in the  $\gamma = 0.7$  cell at  $Ra = 5.5 \times 10^9$ .

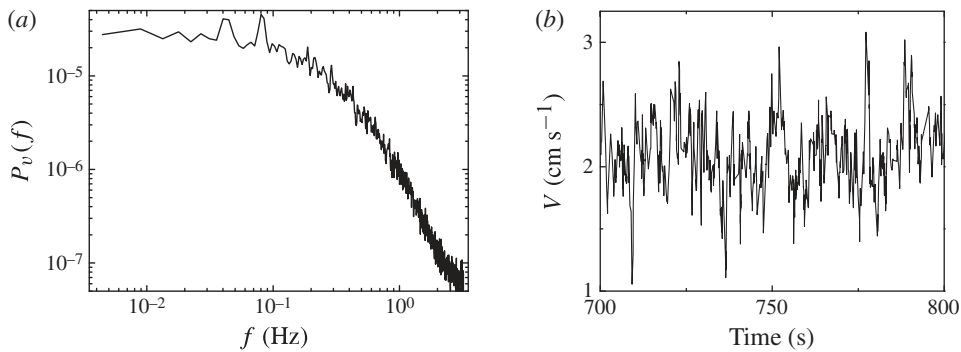


FIGURE 8. (a) Measured power spectrum  $P_v(f)$  of the horizontal velocity  $V_h(t)$  in the  $\gamma = 0.5$  cell at  $Ra = 5.5 \times 10^9$ . (b) Time series data of the measured  $V_h(t)$ .

the  $\gamma = 0.5$  cell, which fluctuates around a mean value of  $2 \text{ cm s}^{-1}$ . Figure 8(a) shows the power spectrum  $P_v(f)$  of  $V_h(t)$ . Two frequency peaks are observed in  $P_v(f)$ ; the dominant peak is located at  $0.08 \text{ Hz}$  and the second peak is located at  $0.04 \text{ Hz}$ . The dominant peak ( $0.08 \text{ Hz}$ ) corresponds to the periodic switching of the LSC orientation. This frequency is twice as large as that obtained by the floater ( $0.04 \text{ Hz}$ ), because  $V_h$  cannot tell the difference between  $+$  and  $-$  (see figure 6a). In the actual velocity measurements, however, minor misalignment in the LDV set-up may exist, which will result in a small difference in  $V_h$  between the two angular positions  $+$  and  $-$ . Such a misalignment will give rise to a weak oscillation signal in  $P_v(f)$  at  $0.04 \text{ Hz}$  and possibly also at  $0.08 \text{ Hz}$  (harmonics).

It is seen from figure 4 that the switching period  $t_0$  remains approximately the same as the LSC turnover time  $\tau_t$  in the SDS phase. When  $\gamma$  approaches the lower phase boundary  $0.16$ , the switching signals of both the local velocity and floater become very weak. In fact, in the range  $0.16 < \gamma < 0.20$ , the floater shows no oscillation and we cannot tell whether the oscillations in the velocity signal are from the 2DR phase or from the SDS phase. Therefore, we consider  $0.16 < \gamma < 0.20$  as a transition region between the two phases.

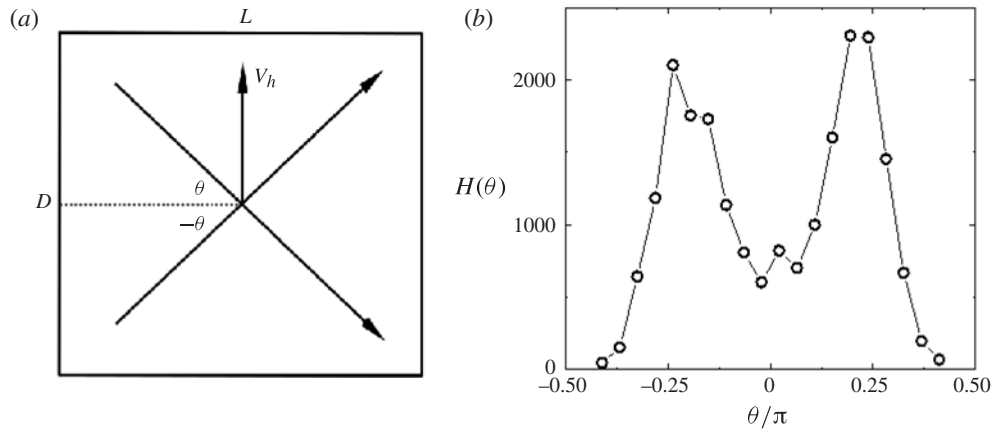


FIGURE 9. (a) Angular position of the rotation plane of the LSC in the LDS phase (top view). When analysing the LDS state, we redefine the  $\theta = 0$  position to be at the centre of the flat sidewall. The arrows indicate the two diagonal orientations of the LSC in the LDS phase. The rectangular box depicts the cross-sectional area at the middle height of the horizontal cylinder with  $L$  being the length of the cell and  $D$  being its diameter. (b) Measured histogram  $H(\theta)$  of the LSC orientation in the  $\Gamma = 1.0$  cell at  $Ra = 5.5 \times 10^9$ . The solid line is drawn to guide the eye.

The LSC in the SDS phase exhibits interesting new dynamics, which have not been observed in the upright cylinders. The fact that the normalized switching period  $t_0/t_s$  is unity suggests that the driving force of the switching dynamics scales with  $V_h/D$ . To compare with turbulent convection in the  $\Gamma = 1$  upright cylindrical cells, we also measured the Nusselt number  $Nu$  and Reynolds number  $Re$  as a function of  $Ra$  (Song & Tong 2010). In the  $\Gamma = 0.5$  cell, for example, we found that the measured  $Nu(Ra)$  can be well described by an effective power law,  $Nu = 0.25Ra^{0.27}$ . The measured  $Re(Ra)$  is also found to have a power-law form,  $Re = 0.02Ra^{0.55}$ . These results reveal that besides the new LSC dynamics, the convective flow in the SDS phase possesses other key features of turbulent convection, which are independent of cell geometry and have been observed in the  $\Gamma = 1$  upright cylinders (Ahlers *et al.* 2009b).

### 3.4. Large- $\Gamma$ diagonal switching

Figure 4 reveals that the normalized switching period  $t_0/t_s$  undergoes a sharp increase from  $\Gamma = 1$  to over 5 when  $\Gamma$  becomes larger than the transition aspect ratio  $\Gamma_c = 0.82$ . In the LDS phase ( $\Gamma > \Gamma_c$ ), we find that the rotation plane of the LSC still oscillates between the two diagonals of the cell but the oscillation span is no longer across the curved sidewall, as indicated in figure 6(a), rather across the flat end wall, as shown in figure 9(a). Thus, when analysing the LDS state we redefine  $\theta = 0$  at the centre of the flat sidewall, as shown in figure 9(a). Figure 9(b) shows the measured histogram  $H(\theta)$  of the LSC orientation using the rotating floater. The measured  $H(\theta)$  reveals two most probable (peak) positions at  $\theta = \pm \pi/4$ , which coincide with the angular position of the two longest diagonals of the  $\Gamma = 1.0$  cell.

The sharp transition at  $\Gamma_c = 0.82$  can be explained as follows. As shown in figure 10, the shortest distance between the two ends of the conducting plate is  $\overline{AB} = (\sqrt{3}/2)D = 0.86D$ . We take this length as the span across which the rotation plane of the LSC switches periodically in the LDS phase. On the other hand, the span of the LSC

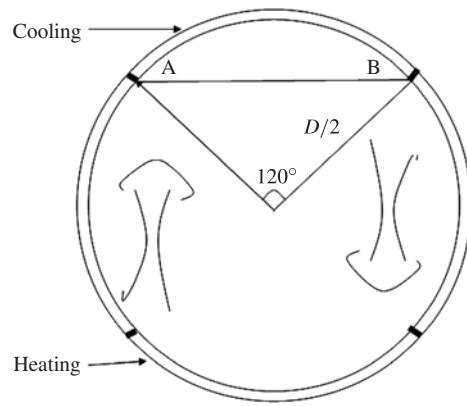


FIGURE 10. End view of the horizontal cylinder with the length  $\overline{AB}$  between the two ends of the conducting plate being  $(\sqrt{3}/2)D$ .

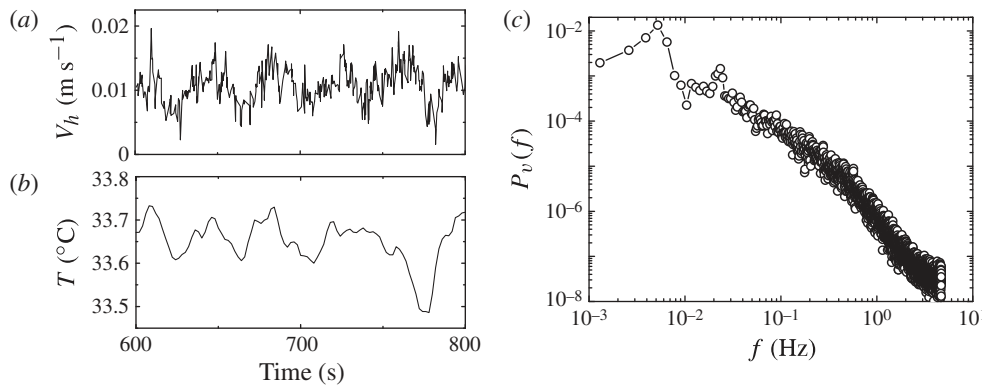


FIGURE 11. (a) Measured local velocity  $V_h(t)$  as a function of time  $t$  at 1 cm above the centre of the bottom conducting plate. (b) Time series data of the local temperature at the mid-height of the cell, 1.5 cm away from the curved sidewall. (c) Measured power spectrum  $P_v(f)$  (open circles) of  $V_h(t)$  in (a). The solid line is drawn to guide the eye. All of the measurements are made in the  $\Gamma = 1.0$  cell at  $Ra = 5.5 \times 10^9$ .

oscillation in the SDS phase is across the cell length  $L$ , as indicated in figure 6(a). The two spans become equal when  $\Gamma = 0.86$ . The sharp transition between the SDS and LDS phases, therefore, suggests that the rotation plane of the LSC tends to oscillate between the two diagonals of the cell with the shortest span possible. In the SDS phase ( $\Gamma < 0.82$ ), the shorter span is across the curved sidewall of length  $L$ , whereas in the LDS phase ( $\Gamma > 0.82$ ), the shorter span is across the flat end wall.

As indicated in figure 9(a), when the LSC rotation plane switches from one diagonal to the other, the measured  $V_h(t)$  will change its sign from being positive to negative (or vice versa). Similarly, the temperature probe near the mid-point of the sidewall can also detect the alternative changes of warm and cold plumes passing through the region. Indeed, the periodic switching of the LSC orientation is observed from the local velocity and temperature measurements, as shown in figure 11(a,b). Figure 11(c) shows the power spectrum  $P_v(f)$  (open circles) of the measured  $V_h(t)$ . Two frequency

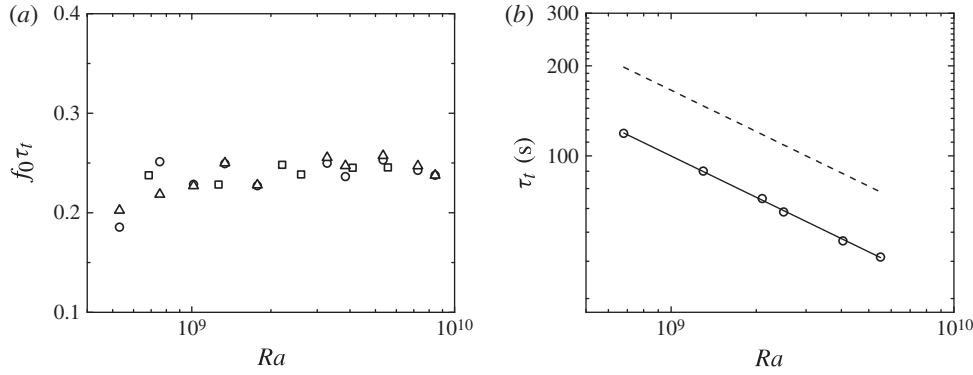


FIGURE 12. (a) Normalized switching frequency  $f_0 \tau_t$  by the LSC turnover time  $\tau_t$  as a function of  $Ra$  in the  $\Gamma = 1.0$  horizontal cylinder. The frequency is obtained using three different methods: temperature (circles), velocity (squares) and floater (triangles). (b) Measured LSC turnover time  $\tau_t$  as a function of  $Ra$  in the  $\Gamma = 1.0$  horizontal cylinder. The solid line is a power-law fit to the data,  $\tau_t = aRa^{-0.46}$ , with  $a = 1.34 \times 10^6$  and  $-0.46 \pm 0.02$ . The dashed line indicates the measured  $\tau_t$  in the  $\Gamma = 1.0$  upright cylinder (Qiu & Tong 2002):  $\tau_t = 2.29 \times 10^6 Ra^{-0.46}$ .

peaks are observed in  $P_v(f)$ . The dominant peak at  $f_0 = (5.2 \pm 0.65) \times 10^{-3}$  Hz corresponds to the switching frequency of the LSC orientation and is the same as that obtained by using the floater. The second peak at  $f_1 = (2.2 \pm 0.065) \times 10^{-2}$  Hz is approximately 4.2 times larger than  $f_0$  and thus is not a simple harmonic of the first peak. It results from the wiggling of the LSC rotation plane around the corner of the longest diagonals of the cell. Since this oscillation frequency is faster than the turnover frequency, it must be different from the advected sloshing and twisting oscillations previously observed in  $\Gamma = 1$  upright cylinders (Funfschilling & Ahlers 2004; Xi *et al.* 2006; Brown & Ahlers 2009).

Figure 12(a) shows the measured switching frequency  $f_0$  as a function of  $Ra$  in the  $\Gamma = 1$  cell. In the plot,  $f_0$  is normalized by the LSC turnover time  $\tau_t$ . The switching frequencies obtained using three different methods superpose with each other and remain approximately constant in the  $Ra$  range studied. Figure 12(a) thus reveals that  $f_0$  has the same  $Ra$  dependence as  $1/\tau_t$  does. Figure 12(b) shows the measured  $\tau_t$  as a function of  $Ra$  in the  $\Gamma = 1$  cell. The data are well described by a power law,  $\tau_t = aRa^{-0.46}$ , with  $a = 1.34 \times 10^6$  and  $-0.46 \pm 0.02$  (solid line). For comparison, we also plot in figure 12(b) the measured  $\tau_t$  in the  $\Gamma = 1$  upright cylinder (Qiu & Tong 2002),  $\tau_t = 2.29 \times 10^6 Ra^{-0.46}$  (dashed line). The obtained value of  $-0.46$  in the  $\Gamma = 1$  horizontal cylinder agrees well with the value obtained in the  $\Gamma = 1$  upright cylinder. In figure 4, we have shown that the normalized switching period,  $t_0/\tau_t = 1/(f_0 \tau_t)$ , does not change much with  $Ra$ . Figure 12(a) further confirms that the measured  $t_0/\tau_t$  (or  $f_0 \tau_t$ ) is indeed invariant with  $Ra$  in the  $Ra$  range studied. It is also found that the wiggling frequency  $f_1$  discussed above has the same  $Ra$ -dependence as  $f_0$  does (Song 2011).

There is a clear distinction between the SDS and LDS phases. In the SDS phase, one finds the normalized switching period  $t_0/(D/V_h) \approx 1$  for all values of  $\Gamma$ , whereas in the LDS phase,  $t_0/(D/V_h)$  is found to be strongly dependent on  $\Gamma$ . Figure 13 shows the measured  $t_0/(D/V_h)$  as a function of the reduced aspect ratio  $\Gamma = (c - c_c)/c$ , where  $c_c = 0.82$  is the transition aspect ratio between the SDS and LDS

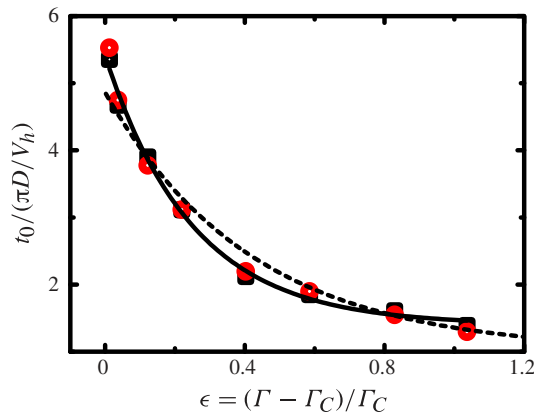


FIGURE 13. (Colour online) Normalized switching period  $t_0/(\pi D/V_h)$  as a function of the reduced aspect ratio  $\epsilon = (\Gamma - \Gamma_C)/\Gamma_C$ . The measurements are made at 1 cm above the centre of the conducting plate with  $Ra = 2.7 \times 10^9$  (circles, shown in red online) and  $5.5 \times 10^9$  (black squares). The solid line is an exponential fit to the data:  $t_0/(\pi D/V_h) = 1.4 + 4e^{-\epsilon/0.25}$ , with  $\tau_0 = 0.25$ . The dashed line is another exponential fit:  $t_0/(\pi D/V_h) = 1 + 3.86e^{-\epsilon/0.42}$ , with  $\tau_0 = 0.42$ .

phases. The two sets of data obtained at two different values of  $Ra$  superpose with each other and can be fit by an exponential decay function,  $t_0/(\pi D/V_h) = 1.4 + 4e^{-\epsilon/0.25}$ , with  $\tau_0 = 0.25$  (solid line). The data could also be fit to a function,  $t_0/(\pi D/V_h) = 1 + 3.86e^{-\epsilon/0.42}$ , with  $\tau_0 = 0.42$  (dashed line), where the constant is fixed so  $t_0/(\pi D/V_h)$  decays to unity when  $\epsilon$  becomes very large. It is seen from figure 13 that the dashed line fits the data less well than the solid line.

### 3.5. Periodic rocking

In the LDS phase, the temperature distribution along the curved sidewall is not uniform. For example, if the fluid temperature at position B shown in figure 14(a) is colder, the fluid temperature at position C (near the opposite end of the cell) will be warmer due to the heat transport by the LSC. At position O, the fluid temperature oscillates following the switching of the LSC orientation. When  $\epsilon = 1.3$ , we find that the fluid temperature at positions B, C and O sometimes becomes fully synchronized. Figure 14(b) and (c) show the temperature time series data simultaneously taken at positions B, C and O. During the time period 500–2000 s (labelled as PR), the temperature signals at the three positions oscillate in phase at a low frequency. In the time period 4500–6500 s (labelled as LDS), the temperature signals at positions B and C oscillate out of phase at a higher frequency. By carefully examining the temperature time series data of the top and bottom conducting plates as shown in figure 15(a,b), we find that the mean temperature of the conducting plates along the sidewall remains the same pattern with one side of the cell being warmer than the other side. Temperature oscillations in the conducting plates also become fully synchronized within each plate in the time period 500–2000 s (labelled as PR). The amplitude of these synchronized temperature oscillations is larger than those in the time period 4500–6500 s (labelled as LDS). The spatial synchronization of the temperature oscillation along the sidewall and along the conducting plates suggests the emergence of a new flow state with the bulk fluid as a whole rotating back and

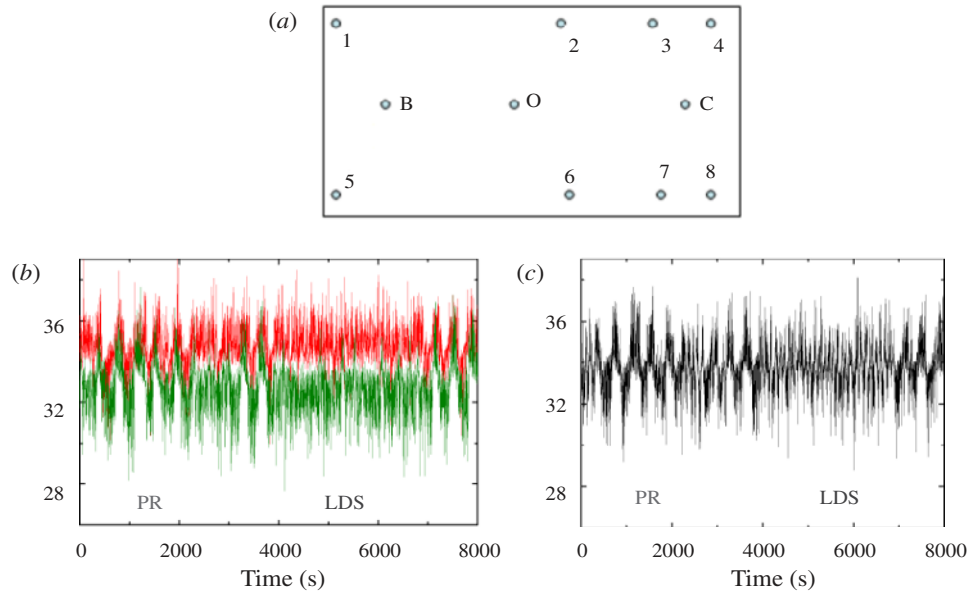


FIGURE 14. (Colour online) (a) Positions of the local temperature measurement near the curved sidewall (side view). The top and bottom four points (numbered 1–8) indicate the positions of the thermistors embedded inside the top and bottom conducting plates. The middle three points (B, O and C) indicate the positions at which the local fluid temperature is measured (15 mm away from the curved sidewall, on the same side, and at the same height). Positions B and C are  $D/4$  (with  $D$  being the cell diameter) away from the end. Position O is  $0.75D$  away from one side and  $0.94D$  away from the other side. (b) Temperature signals at positions B (lower curve, shown in green online) and C (upper curve, shown in red online). (c) Temperature signal at position O. Measurements are made in the  $\Gamma = 1.69$  cell at  $Ra = 5.5 \times 10^9$ .

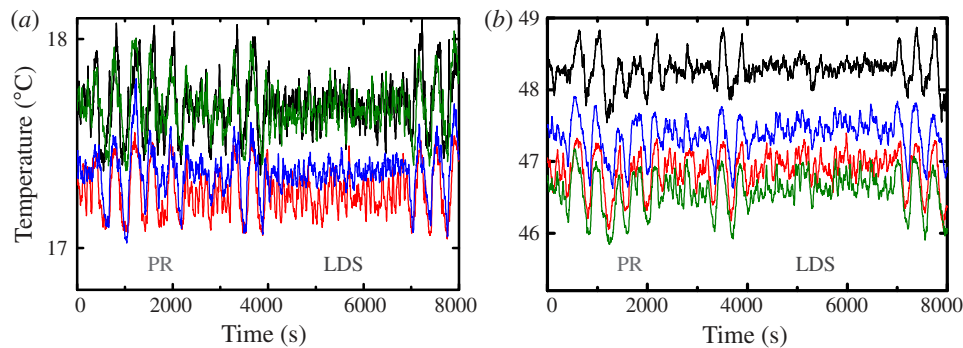


FIGURE 15. (a) Temperature signals of the top conducting plate at positions 1 (black), 2 (green), 3 (blue) and 4 (red). (b) Temperature signals of the bottom conducting plate at positions 5 (black), 6 (green), 7 (blue) and 8 (red). Measurements shown are made simultaneously with those shown in figure 14 in the  $\Gamma = 1.69$  cell at  $Ra = 5.5 \times 10^9$ .

forth (rocking) around the central axis of the horizontal cylinder. Therefore, we name this new phase as PR.

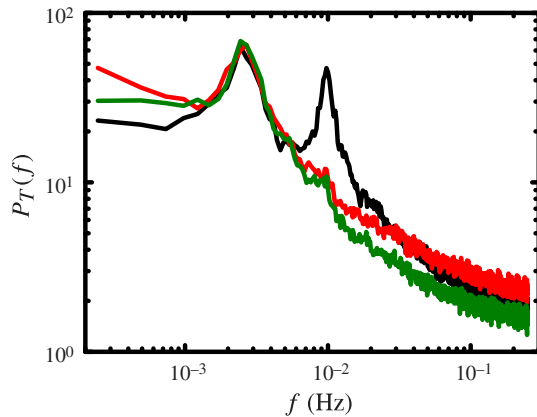


FIGURE 16. Measured power spectra  $P_T(f)$  of local temperature fluctuations at positions B (green), O (black) and C (red) as shown in figure 14.

Figure 16 shows the power spectra  $P_T(f)$  of the measured fluid temperature at positions B (shown in green online), O (black) and C (shown in red online). The dominant peak at  $f_0^{PR} = 2.5 \times 10^{-3}$  Hz corresponds to the PR, which is observed at all three positions. The second peak at  $f_0^{LDS} = 0.01$  Hz, which is only observed at position O (black curve), corresponds to the LDS phase. Near the two flat end walls of the cell (positions B and C), temperature oscillations due to the periodic switching of the LSC orientation are much weaker than that in the middle region of the cell (position O). Therefore, the measured  $P_T(f)$  at positions B and C do not show a LDS peak. For cells with  $1.3 < \gamma < 1.69$ , the LDS phase and PR phase coexist and they compete with each other. It appears that the two flow modes changes randomly inside the cell. In the  $\gamma = 1.69$  cell (without a piston), the ratio of time occupied by the PR phase to that by the LDS phase is  $60/40$ .

Figure 17(a) shows the normalized rocking period  $t_R/t_i$  as a function of  $\gamma$  at  $Ra = 5.5 \times 10^9$ . The solid line is a linear fit,  $t_R/t_i = -5.2 + 6.2 \gamma$ . For comparison, we plot in figure 17(b) the measured  $\gamma$ -dependence of the LSC turnover time  $t_i$  at the same value of  $Ra$ . It is seen that the LSC turnover time  $t_i$  has a much weaker  $\gamma$ -dependence compared with the rocking period  $t_R$ . By comparing figures 17(a) and 4 one finds that the rocking period  $t_R$  has a different  $\gamma$ -dependence from that of the switching period  $t_0$ ;  $t_R$  increases linearly with  $\gamma$  whereas  $t_0$  decreases exponentially with  $\gamma$ . This finding indicates that the two flow modes are driven by different mechanisms. We also studied the  $Ra$ -dependence of  $t_R$  (Song 2011). It was found that  $t_R = 0.7Ra^{-\nu_{PR}}$  with  $\nu_{PR} = 0.48$ . This value of  $\nu_{PR}$  is very close to the value obtained for the LSC turnover time  $t_i$  (see figure 12b).

#### 4. Theoretical analysis

Brown & Ahlers (2007, 2008a,b) proposed a stochastic model that explains many aspects of the LSC dynamics in the upright cylinders. In the Brown–Ahlers model, the dynamics of the azimuthal orientation  $\theta(t)$  of the near-vertical rotation plane of the LSC is described by a (damped) diffusive process in a potential. The equation of motion is

$$\ddot{\theta} + \frac{\dot{\theta}}{\tau} = -U_x(\theta) + f(t). \tag{4.1}$$

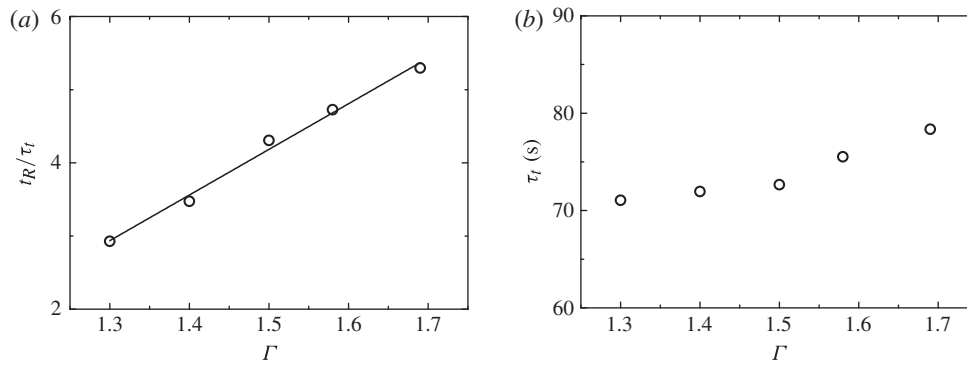


FIGURE 17. (a) Normalized rocking period  $t_R / \tau_t$  by the LSC turnover time  $\tau_t$  as a function of  $\Gamma$  at  $Ra = 5.5 \times 10^9$ . The solid line is a linear fit,  $t_R / \tau_t = -5.2 + 6.2 \Gamma$ . (b) Measured LSC turnover time  $\tau_t$  as a function of  $\Gamma$  at  $Ra = 5.5 \times 10^9$ .

The damping time scale  $\tau_t$  is associated with the rotational inertia of the LSC. The stochastic term  $f(t)$  represents a driving due to turbulent fluctuations, and is modelled as Gaussian distributed white noise with strength characterized by a diffusivity  $D$  such that the mean-square change in rotation rate is  $\langle \dot{\theta}^2 \rangle = D \cdot t$  in the limit of  $t \rightarrow 0$ , where  $t$  is the delay time. The properties of  $\theta$  and dynamics due to the damping and stochastic terms have been studied in detail with experiments in upright cylinders (Brown & Ahlers 2008a). Motivated by these earlier experiments, the potential term  $U_x(\theta)$  was predicted to be due to the pressure from the sidewall and produces an azimuthal forcing as a function of the sidewall shape. The subscript  $x$  is used as a placeholder for different model potentials which will be identified by different subscripts.

In the upright cylinders used in the original experiments (Brown & Ahlers 2008b), the potential was uniform due to the azimuthal symmetry of the cell. For an idealized LSC of approximately zero width in an upright cylindrical cell with no vertical variation in wall shape, but with a non-circular cross-section with mean diameter  $D(\theta)$  equal to its height  $H$ , the potential was given by (Brown & Ahlers 2008b)

$$U_u(\theta) = \frac{2H^2}{2D(\theta)^2}, \quad (4.2)$$

where  $\omega = 2 / \tau_t$  is the LSC turnover frequency. An important feature of (4.2) is that the potential is a simple function of the geometry, in terms of the orientation-dependent diameter  $D(\theta)$  in a horizontal cross-section of the cell.

We now test the applicability of this model to a different geometry, namely, the horizontal cylinder. We will calculate the potential based only on the horizontal cross-section at the mid-height of the cell without taking into account the vertical variation of the horizontal cross-section. We will first keep the approximation of a zero-width LSC, and in later sections we will introduce a modification to the potential for a LSC of non-zero width.

Figure 18 shows the top view of the horizontal mid-height cross-section of a  $\Gamma > 0.82$  cell, with  $L$  being the length of the curved sidewall and  $D$  being the length of the flat end wall. Line  $\overline{BF}$  represents the LSC plane with diameter equal to the length of  $\overline{BF}$  and orientation  $\theta(t)$  with respect to  $\overline{OA}$ , centred at the middle of an end wall.

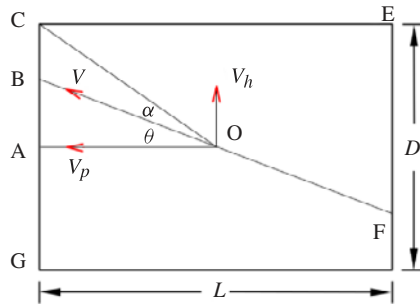


FIGURE 18. (Colour online) Top view of the horizontal cross-section of a  $\Gamma$  cell at the mid-height. Line  $\overline{BF}$  represents the instantaneous LSC orientation  $\theta$  with respect to line  $\overline{OA}$ , and its length is the azimuthally varying diameter  $D(\theta)$  with the angle  $\theta$  being defined with respect to the diagonal line  $\overline{OC}$ . The three arrows (shown in red online) indicate the velocity coordinate system used in the LDV measurement.

The potential in (4.2) still needs to be modified to account for the variation of the mean horizontal diameter with  $\theta$ , as that equation assumed the average horizontal diameter was equal to the height of the container. The factor  $H/D(\theta)$  in (4.2) represents the ratio of the mean LSC diameter over the diameter of a horizontal cross-section along the sidewall. The overall diameter of the LSC can be estimated as the geometric mean of the end cap diameter  $D$  and the maximum horizontal diameter  $D_m = D \sqrt{1 + \Gamma^2}$  (Niemela & Sreenivasan 2003), so we make the substitution  $H = D \sqrt{1 + \Gamma^2}/2$ . We rewrite the potential for the horizontal cylinder with the approximation of a zero-width LSC as

$$U_h = \frac{C(\theta) D_m^2}{2D(\theta)^2}, \quad (4.3)$$

where  $C(\theta) = (1 + \Gamma^2/2)/(1 + \Gamma^2)$  is a dimensionless factor dependent on aspect ratio, and its value varies between 1 and 0.5 due to the changing vertical aspect ratio of the cell. Since this is a weak variation, and there are significant other differences in the geometry of the horizontal cylinders at different aspect ratios that have not been modelled yet, we are not able to test the accuracy of  $C(\theta)$  or attribute any significant physics to it at this time.

For the convenience of later expanding around the potential minimum in the corners, we alternately define the LSC orientation  $\theta$  relative to the nearest diagonal. As shown in figure 18,  $\theta$  is related to  $\theta$  via the equation  $\theta = \arctan(\Gamma^{-1}) - \theta$ . The diameter function  $D(\theta) = \overline{BF}$  is given by Brown & Ahlers (2008a) as

$$D_{\pm}(\theta) = \frac{D_m}{|\cos \theta + \pm \Gamma \sin \theta|}, \quad (4.4)$$

where  $D_+(\theta)$  stands for the diameter  $D(\theta)$  when  $\theta$  is along the flat end wall (on the left side of the diagonal line  $\overline{OC}$  in figure 18) and  $D_-(\theta)$  is the diameter when  $\theta$  is centred along the curved sidewall (on the right side of  $\overline{OC}$ ).

#### 4.1. Probability distribution of the LSC orientation for a zero-width LSC

In this subsection, we test the validity of the potential in (4.3) for a zero-width LSC in the horizontal cylinders. This is done by comparing the measured probability

distribution of the LSC orientation  $P(\theta)$  to a model prediction. In the strong-damping limit of (4.1), evaluating the Fokker–Planck equation (Gitterman 2005; Brown & Ahlers 2008b) results in a prediction for the probability distribution

$$P_x(\theta) \propto \exp\left[-\frac{U_x(\theta)}{D \cdot \tau}\right] = \exp\left[-\frac{U_x(\theta)}{U_0}\right], \quad (4.5)$$

where the rightmost expression is rewritten in terms of dimensionless quantities. The factor  $U_0 = 2 \cdot D \cdot \tau^{-2}$  is a dimensionless ratio of kinetic to potential energy scales independent of the cross-section shape. The geometry dependence for the potential  $U_h$  is given by

$$U_h(\theta) = \frac{C(\theta) D_m^2}{D(\theta)^2} = C(\theta) \times (|\cos \theta| + |\sin \theta|)^2. \quad (4.6)$$

Combining (4.5) and (4.6) leads to a prediction for  $P(\theta)$  for a zero-width LSC in the horizontal cylinder. The main feature of this function is that the longest diameter corresponds to the lowest potential and thus the highest probability, which generally agrees with our data shown in figure 9(b) as well as previous experiments in rectangular geometries (Zocchi, Moses & Libchaber 1990; Daya & Ecke 2001; Zhou *et al.* 2007).

To test this model, we obtain higher-resolution data for  $\theta(t)$  than those shown in figure 9(b). Because the response time of the floater is not fast enough to accurately determine the instantaneous value of  $\theta(t)$  near the diagonal positions of the cell (small values of  $\theta$  as shown in figure 18), we use the velocity data to compute  $P(\theta)$ . In the experiment, we use the angle  $\theta$  to describe the LSC orientation. The three arrows (shown in red online) in figure 18 represent the velocity coordinate system used in the LDV measurement. Our LDV measurements can only give the horizontal velocity  $V_h$  parallel to the flat end wall of the cell and the measuring position is located at 14 mm above the centre of the bottom conducting plate. This is a symmetric location in the cell, which always stays in the LSC rotation plane. From figure 18 one finds that  $V_h = V_p \tan \theta$ , where  $V_p$  is the velocity component perpendicular to the end wall of the cell. While  $V_p$  is not directly measured in the experiment, one can obtain its value when the LSC orientation is aligned along the cell diagonal, at which  $V_h$  takes its most probable value  $V_m$  and thus one has  $V_m = V_p \tan \theta_0$  with  $\tan \theta_0 = 1$ . Assuming  $V_p$  does not change very much with  $\theta$ , we have  $V_p = V_m$ . Therefore, the LSC orientation  $\theta$  is given by

$$\theta = \arctan(V_h/V_p) = \arctan[V_h/(V_m)]. \quad (4.7)$$

In figure 19 we plot a direct comparison between the prediction of (4.5) and (4.6) and the measured  $P(\theta)$  in the  $\ell = 1.2$  cell. While the peaks of  $P(\theta)$  are located near the cell corners as predicted, this model  $P_h(\theta)$  predicts sharp peaks at the corners due to the sharp corners of the cross-section, a discrepancy with the measured smooth peaks shown in figure 19.

#### 4.2. Correction for the finite width of the LSC

In this subsection, we correct the discrepancy in  $P(\theta)$  near the corners of the cell by introducing a correction to the potential to account for the width of the LSC. This

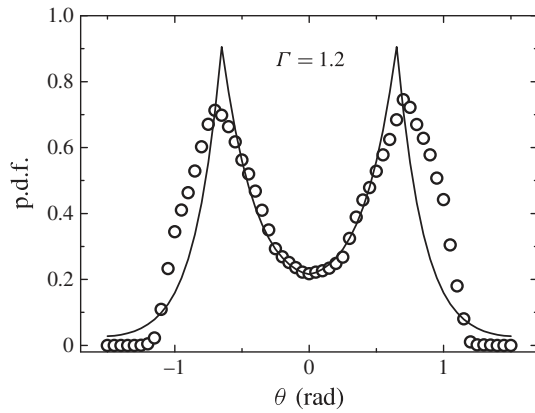


FIGURE 19. Comparison between the measured p.d.f.  $P(\theta)$  (open circles) and the calculated  $P_h(\theta)$  using (4.5) and (4.6) for a zero-width LSC (solid line). The value of  $U_0$  in (4.5) is chosen to fit to the data. The measurements are made in the  $\Gamma = 1.2$  cell at  $Ra = 5.5 \times 10^9$ .

discrepancy near the corners can be attributed to the model assumption of relatively small variations in the cross-section diameter of the cell, which becomes invalid at the sharp corners. The original model of Brown & Ahlers (2008b) approximated the LSC to be of zero width so that the pressure forcing from the sidewall depended only on the slope of the diameter function at  $\theta$ . However, for a LSC with a finite angular width  $\Delta\theta$  and non-negligible variations in  $D(\theta)$  over the width  $\Delta\theta$ , the sidewall provides different forces along the width of the LSC. The net forcing from the sidewall could be modified by smoothing the potential over the range of  $\Delta\theta$ . Assuming a uniform weighting, the potential can be modified by averaging over the width of  $\Delta\theta$ :

$$U = C(\theta) \frac{D_m^2}{D(\theta)^2} = C(\theta) \frac{1}{\Delta\theta} \int_{\theta - \Delta\theta/2}^{\theta + \Delta\theta/2} \frac{D_m^2}{D(\theta')^2} d\theta'. \quad (4.8)$$

Since this smoothing will have the largest effect near the corners, we characterize the potential near the corners by a first-order expansion in  $\theta$  around a corner. The first-order expansion of the diameter in (4.4) yields  $D_m^2/D(\theta)^2 = (1 + 2\theta \pm 1|\theta|)$ . Integrating (4.8) up to second order yields

$$U = C(\theta) \left[ 1 + (\theta + \theta^{-1}) \frac{\Delta\theta}{4} + (\theta - \theta^{-1}) \frac{\Delta\theta^2}{2} \right]. \quad (4.9)$$

This smoothed potential with  $\Gamma = 1.2$  (black solid line) is shown in comparison to the unsmoothed potential  $U_h$  (see (4.6); dashed line, shown in red online) in figure 20. In the plot, the solid line is obtained using (4.9) for  $|\theta| < \Delta\theta/2$ , and (4.6) is used elsewhere. We choose the value  $\Delta\theta = \pi/10$  as a fixed parameter for all of our analysis. With this small value of  $\Delta\theta$ , the second-order expansion in  $U(\theta)$  remains within 2% of the exact calculation, and this produces enough smoothing to better fit the data in figure 20. The calculated potentials have two wells for  $-\Delta\theta/2 < \theta < \Delta\theta/2$  and are repeated over the full range of  $2\pi$ . The potential minima correspond to the diagonals of the cell, and there is a potential barrier in between the closer corners

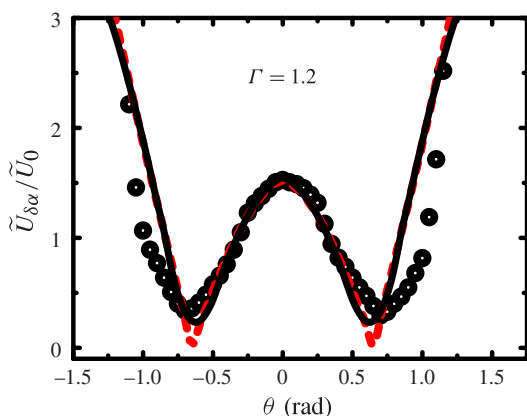


FIGURE 20. (Colour online) Comparison between the smoothed potential  $U_{\delta\alpha}/U_0$  from (4.9) (black solid line) and the unsmoothed potential  $U_h/U_0$  from (4.6) (dashed line, shown in red online) for the  $\Gamma = 1.2$  cell. The two calculated potentials are normalized by a constant  $U_0 = 1/3.5$  in order to compare with the measured potential  $U_m(\theta)/U_0$  at  $Ra = 5.5 \times 10^9$  (open circles).

---

	1	1.1	1.2	1.4	1.69
$1/U_0$	3.5	3.5	3.4	2.6	2.1

---

TABLE 1. Fitting results for the measured p.d.f.  $P(\theta)$  with different values of  $\Gamma$ . The fitting uncertainty for  $1/U_0$  is  $\pm 0.1$ .

of a rectangular cell. The correction for the finite width produces a much smoother potential minimum, as shown in figure 20.

Figure 21 shows the measured  $P(\theta)$  in five panels for five different values of  $\Gamma$  in the range 1 to 1.69 (open circles). Also shown are fits of the model prediction using (4.5) and (4.9) with the correction for a non-zero width LSC (solid lines). We used the potential  $U_{\delta\alpha}$  from (4.9) for  $|\theta| < \pi/2$ , and the potential  $U_h$  from (4.6) elsewhere. In each fit,  $U_0$  is the only free fit parameter ( $\Gamma = \pi/10$  is a fixed parameter, and the overall proportionality constant is determined by the normalization requirement), and the least-squares fit is conducted over the angular range between the two probability peaks. The fitted values of  $U_0$  are given in table 1. The measured  $P(\theta)$  shows a slight asymmetry with the peak value of  $P(\theta > 0)$  being slightly larger than that of  $P(\theta < 0)$ . This is observed in figures 19 and 21 as well as in figures 9(b) and 6(b). The slight asymmetry shown in these figures is probably caused by the minute misalignment of the vertical orientation of the horizontal cylinder relative to the direction of gravity. In the experiment, we have tried our best to keep the cell vertically symmetric but imperfections do exist.

The correction for the non-zero width of the LSC results in a significant improvement to the prediction for  $P(\theta)$  compared with that for the sharp potential shown in figure 19. In particular, it captures the curvature of the peaks and more accurately reflects the potential difference between the central minimum and the peak values of  $P(\theta)$ . The model fits the measured  $P(\theta)$  well for the  $\Gamma = 1$  cells, and for

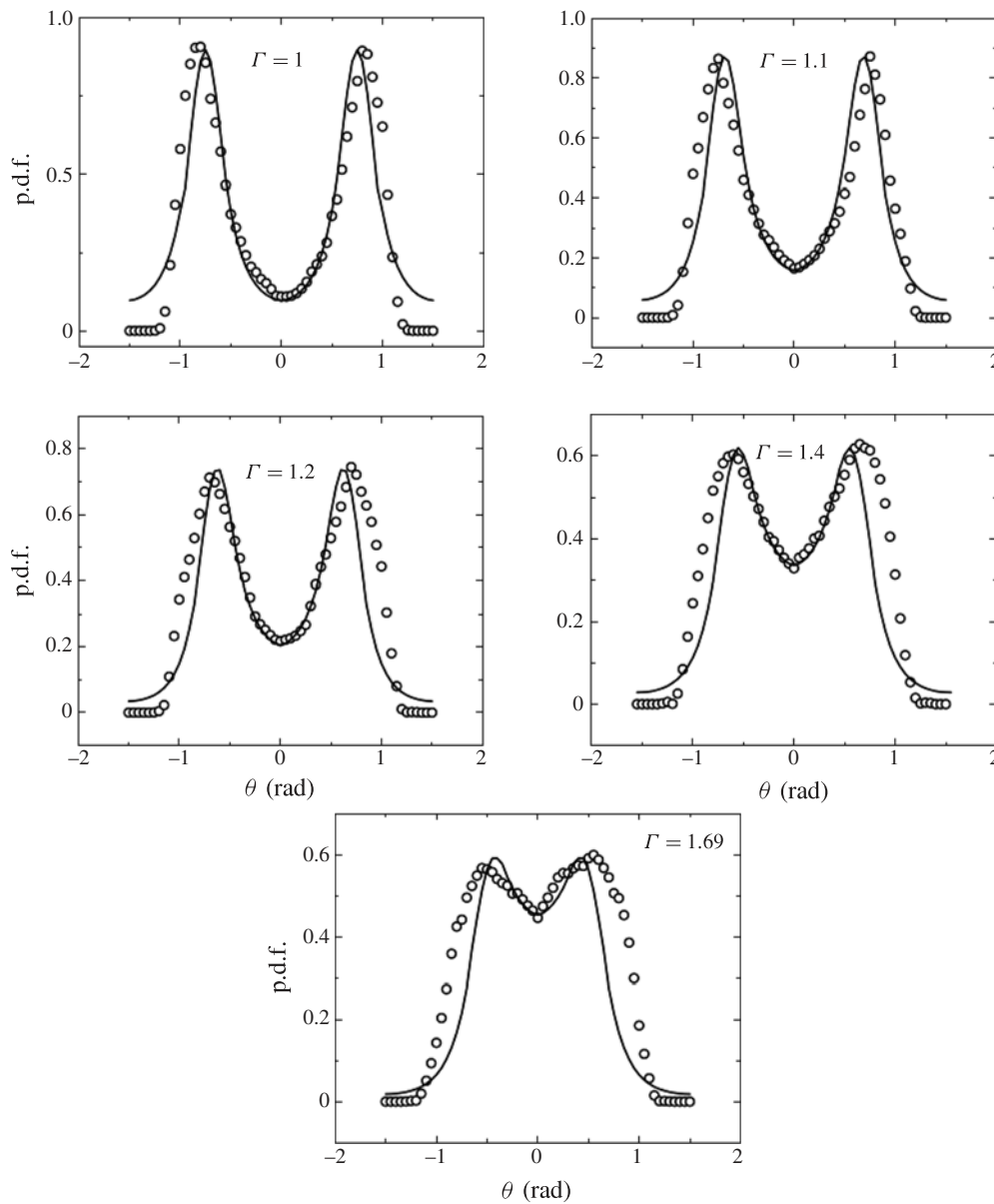


FIGURE 21. Comparison between the measured p.d.f.s  $P(\theta)$  at five values of  $\Gamma$  (open circles) and fits of the model prediction  $P(\theta)$  using (4.5) and (4.9) for a non-zero width LSC (solid lines). The fitting is made using  $U_0$  as a free parameter. The measurements are made at  $Ra = 5.5 \times 10^9$  and the values of  $\Gamma$  are each shown in different panels.

1.2, the values of  $U_0$  remain constant within the uncertainties (see table 1), as expected by the model. For larger values of  $\Gamma$ , the model fits less well, and the best fit values of  $U_0$  start to vary. The model may be less accurate for  $\Gamma$  further from 1 because the model assumptions include a relatively slow variation in  $D(\theta)$  with  $\theta$ , which becomes less accurate at  $\theta$  further from 1. The peak positions of

$P(\theta)$  are measured to be slightly further apart than the nearest corners of the cell, compared with the model prediction which puts the peaks slightly closer together than the corners. This discrepancy could be due to the system being out of the strong-damping limit (which is suggested by the fact that there are steady oscillation modes), or an effect of the curved sidewall, which may provide a smaller restoring force compared with that of a flat sidewall. The tails of  $P(\theta)$  along the longer sidewall are significantly lower than the model prediction. This discrepancy is also likely attributable to the curvature of the sidewall and heater, which are the only source of asymmetry for  $\beta = 1$ .

We compare the model parameters found here for horizontal cylinders with those found for upright cylinders. Using the equation  $U_0 = 2 \cdot D \cdot / \lambda^2$  and the measured values of  $\lambda$ ,  $\nu$  and  $D \cdot$  for a  $\beta = 1$  upright cylinder, we find  $U_0 = 3.7 \times 10^{-2}$  at  $Ra = 5.5 \times 10^9$  (medium cell) (Brown & Ahlers 2008b). This value of  $U_0$  is 7.7 times smaller than the measured  $U_0$  ( $\approx 0.29$ ) in the  $\beta = 1$  horizontal cylinder. This suggests the azimuthal motion is more strongly driven in the horizontal cylinder. While  $\lambda$  and  $\nu$  are physically related to the Reynolds number and not expected to vary with cell geometry (Brown & Ahlers 2008a), it remains unknown how the stochastic driving strength  $D \cdot$  depends on cell geometry and the turbulence microstructure.

Using (4.5) one can directly obtain the potential  $U_m(\theta)/U_0 = -\ln[P(\theta)] + const.$  from the measured  $P(\theta)$ . The circles in figure 20 show the measured potential in the  $\beta = 1.2$  cell in comparison with the predictions of the smoothed potential  $U/U_0$  (black solid line) and the unsmoothed potential  $U_h/U_0$  (dashed line, shown in red online). Here the fitted value of  $U_0 = 1/3.5$  (see table 1) is used for the calculated potentials. The two valleys of the potential correspond to the angular position of the two diagonals of the cell. The middle peak is located at the centre of the flat end wall of the cell. The measured periodic switching of the LSC orientation in the LDS phase corresponds to a periodic hopping between the two potential wells. Figure 20 reveals that the smoothed potential  $U/U_0$  for a non-zero width LSC accurately describes the measured double-well potential, especially in the central barrier region between the two valleys.

To characterize the variation of the potential with  $\theta$ , we consider the potential barrier defined by the potential difference between the minima and maximum in between the closer corners, given by  $U = U_h(\theta = \arctan(\theta^{-1})) - U(\theta = \theta_{min})$  where  $\theta_{min} = (\theta/2)(\theta - \theta^{-1})/(\theta + \theta^{-1})$  is the orientation of the potential minimum. The potential minimum is shifted slightly from zero due to the smoothing from the non-zero width of the LSC. Here  $U$  can be calculated from (4.6) and (4.9),

$$U^\pm = C(\theta) \frac{1}{\pm 2 - \frac{1}{\theta \pm 1}}, \quad (4.10)$$

where  $U^+$  is used for  $\theta > 1$  and  $U^-$  is used for  $\theta < 1$ . A measurement of the potential barrier can be deduced from (4.5) to be  $U_m/U_0 = -\ln[P(\theta = 0)/P(\theta = \arctan(\theta^{-1}) - \theta_{min})]$ . Figure 22(a) compares the measured  $U_m/U_0$  (circles) with the predicted  $U/U_0$  using (4.10) (triangles) for different values of  $\beta$ . The model gives an accurate description of the evolution of the potential barrier height with  $\beta$ . The function  $U_m/U_0 = -0.2084 + 32.40e^{-2.586\beta}$  (solid line) is fit to the data to obtain a function to approximate  $U_m/U_0$ .

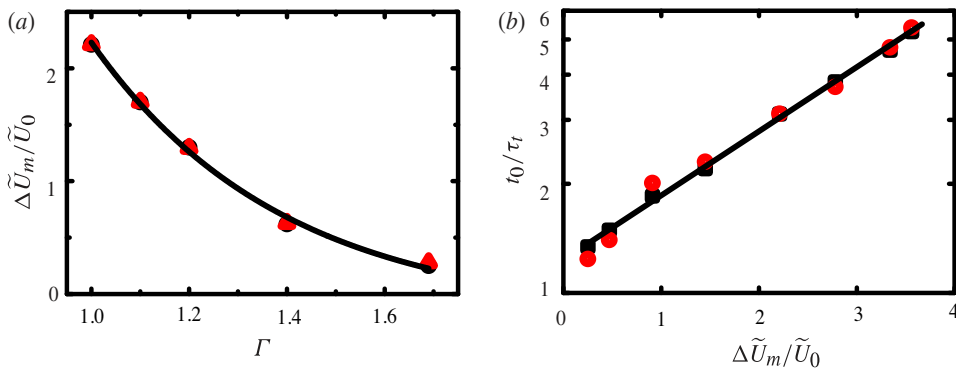


FIGURE 22. (Colour online) (a) Comparison between the measured barrier height  $U_m/U_0$  (black circles) and the calculated  $U_m/U_0$  using (4.10) (triangles, shown in red online) for different values of  $\Gamma$ . The solid line shows the fitted function:  $U_m/U_0 = -0.2084 + 32.40e^{-2.586\Gamma}$ . (b) Measured  $t_0/\tau_t$  in the LDS phase as a function of  $U_m/U_0$ . The circles (shown in red online) are obtained at  $Ra = 2.7 \times 10^9$  and the (black) squares are obtained at  $Ra = 5.5 \times 10^9$ . The solid line shows a fit to (4.11) with  $\beta = 0.395$ .

We now can (re)plot the measured  $t_0/\tau_t$  in the LDS phase (see figure 4) as a function of  $U_m/U_0$ . Figure 22(b) shows the plot and the two symbols are obtained at two different values of  $Ra$ . The data can be well fit to an exponential function (solid line):

$$\frac{t_0}{\tau_t} = 1.265e^{-\beta U_m/U_0}, \tag{4.11}$$

where  $\beta = 0.395$ . Equation (4.11) is of Arrhenius–Kramers type (Arrhenius 1889; Kramers 1940), in which the energy barrier  $U_m$  lengthens the switching period  $t_0$ .

### 4.3. Oscillation frequency around a single corner

The model equation of motion given by (4.1) becomes a second-order linear harmonic oscillator equation for the smoothed potential  $U$  given by (4.9), which applies in the limit of small angular displacements around a corner. In the underdamped regime, such an equation has sinusoidal solutions, where the restoring force comes from the pressure gradient due the variable diameter of the cell. The resonant angular frequency is given by the quadratic term in the potential to be

$$\omega^2 = \frac{2C(\gamma)(\gamma + \gamma^{-1})}{\rho}. \tag{4.12}$$

For  $\gamma = 1/10$  and  $\rho = 1$ , this frequency is  $\omega = 4.8$ , so it is faster than the LSC turnover frequency, with a slight aspect ratio dependence. The predicted oscillation around a single corner, and its higher frequency than the turnover rate agree with the observed wiggling mode shown in figure 11, in which we observed that the frequency  $f_1$  is 4.2 times larger than the turnover frequency.

The restoring pressure from the sidewall comes from the same origin as that which drives the twisting and sloshing oscillations observed in upright cylinders (Brown & Ahlers 2009), but these oscillation modes are distinct because in the latter case advection around the circulation loop slaves the oscillation frequency to the turnover

frequency (Brown & Ahlers 2009). We note that a qualitatively similar oscillation mode around the longest diagonal of a cell has been predicted based on analytical mean flow solutions in an ellipsoid (Resagk *et al.* 2006).

#### 4.4. 2DR: disappearance of the potential barrier at extreme

We observed a transition to 2DR for  $\Gamma = 0.16$ , as shown in figure 4. This transition can be characterized by a change in the shape of  $P(\theta)$  from a single peak in the 2DR phase to two peaks in the SDS mode. Such a transition can be reproduced in the stochastic model with the correction for the finite width of the LSC. As  $\Gamma$  becomes more extreme (either very small or very large compared with 1), the peaks of  $P(\theta)$  get closer together. Due to the smoothing of the potential, the peaks become indistinguishable when they get close enough, effectively merging into a single peak. This occurs when the width  $\Delta\theta$  exceeds the angular distance  $2\theta_p$  between the two peaks. This determines the critical aspect ratios for the transition to be  $\Gamma_c^{\pm 1} = \tan \theta_p = \tan(\theta/2)$ . For  $\theta = \pi/10$ , this yields  $\Gamma_c = 0.16$  and 6.3. The model prediction for the lower  $\Gamma_c$  is in excellent agreement with the observed transition at  $\Gamma_c = 0.16$ , as shown in figure 4. The predicted transition for large aspect ratios ( $\Gamma_c = 6.3$ ) is outside of the measured range.

#### 4.5. Periodic switching in the LDS and SDS phases

The agreement between the measured and predicted  $P(\theta)$  suggests the LSC can be described by the Brown–Ahlers model of a stochastic process in a multi-welled potential. In that model, stochastic switching between corners was predicted on occasions when fluctuations are strong enough to drive the LSC over the potential barrier according to the Arrhenius–Kramers model (Brown & Ahlers 2008*b*). However, in the current experiments, regular oscillations between corners across the lower potential barrier were observed; the SDS state for  $\Gamma < 0.82$  and the LDS state for  $\Gamma > 0.82$ . Regular oscillations in a double-well potential are known, for example, from solutions of the stochastic Duffing oscillator (Dykman *et al.* 1988). In a model of stochastic motion in a double-well potential, regular oscillations between neighbouring corners can occur if either the driving force is at a specific frequency, or white noise can drive oscillations at the resonant frequency of a wider potential. The first case may be possible for example if the LSC switching is excited by another internal oscillation mode such as sloshing or twisting (Brown & Ahlers 2009). However, we do not have measurements of those modes to compare to, so we will consider the latter case.

Since we do not have analytical solutions for periodic oscillations in the wider potential well, we present numerical simulation results to compare with the experimental observations. We use the model equation (4.1) with the potential given by (4.9) for  $|\theta| < \theta/2$  and (4.6) otherwise. The differential equation for  $\theta$  is evolved using a first-order Euler method. The stochastic term  $f(t)$  is generated as a Gaussian distributed random number with standard deviation  $\sqrt{D \cdot \tau/h}$  at each time step separated by time  $h$ . We report simulations with  $h = 0.125$  s, which we confirmed is in the continuum limit and validated the simulations by checking that  $\tau^2 = D \cdot \tau/2$  (Brown & Ahlers 2008*a*). Simulation runs are reported for several aspect ratios  $\Gamma$  in the range of the experiments, lasting  $3 \times 10^6$  s each. The value of  $\tau = 0.12$  s<sup>-1</sup> is set equal to the measured turnover rate at  $\Gamma = 0.83$ .

This numerical model produces regular oscillations between adjacent corners across the lowest potential barriers as observed in the experiments if the stochastic driving

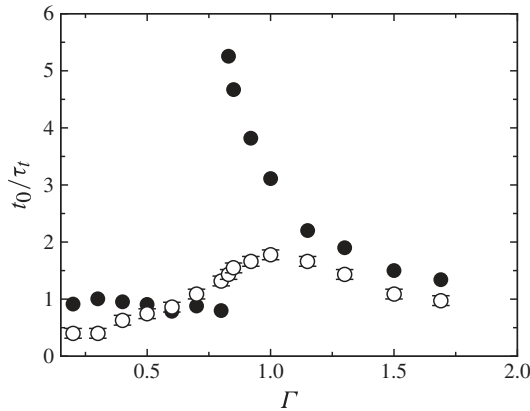


FIGURE 23. A comparison between values of the normalized period  $t_0/\tau_t$  of switching oscillations in the SDS and LDS states as a function of aspect ratio  $\Gamma$ . Solid circles: experimentally measured. Open circles: numerical solutions of the resonant frequency obtained from the Brown–Ahlers model for a rectangular cross-section with parameter values explained in the text.

provides enough kinetic energy to regularly cross the potential barrier ( $D\dot{\phi} > U$ ) and if the system is underdamped ( $\dot{\phi} > 1/\tau$ ), analogous to the stochastic Duffing oscillator (Dykman *et al.* 1988). For smaller  $\dot{\phi}$  the switching oscillation mode becomes overdamped, and the switching between adjacent corners is irregular. The oscillation period is obtained by first calculating a histogram of the time between switchings between corners. In the overdamped regime, the irregular switching produces a peak at zero time. If the peak of this histogram is at a non-zero time, we consider the switching to be dominated by a periodic mode and take that peak time as the oscillation period  $t_0$ .

Simulation results for the oscillation period  $t_0$  are normalized by the turnover time  $\tau_t$  plotted as a function of the aspect ratio  $\Gamma$  in figure 23. Results are shown for a value of  $U_0 = 1/3.5$ , matching the experimentally obtained value for  $\Gamma = 1$ . We chose  $\dot{\phi} = 75$  s which is just large enough to be in the underdamped regime. These values require  $D\dot{\phi} = U_0^2/2 \dot{\phi} = 2.7 \times 10^{-5}$  s<sup>-3</sup>. Regular oscillations are observed across the smallest potential barrier, corresponding to the SDS phase for  $\Gamma < 1$  and the LDS phase for  $\Gamma > 1$ . The oscillation period is longest at  $\Gamma = 1$  where the potential barrier is largest and slows the oscillation, and the period decays to either side as the potential barriers become smaller.

The parameter value of  $\dot{\phi} = 75$  s is about an order of magnitude higher than that measured in upright cylindrical containers (Brown & Ahlers 2008a). Results for this larger value are reported because the variable LSC speed was found to reduce the effective damping just enough to move the system state from the overdamped regime to the underdamped regime for other oscillation modes (Brown & Ahlers 2009), and  $\dot{\phi} = 75$  s is just large enough to be in the underdamped regime. As long as the system is in the underdamped state, the oscillation period is not significantly dependent on  $\dot{\phi}$  if  $U_0$  is held constant. We also note that for this value of  $\dot{\phi}$  and  $U_0$ , the values of the other model parameters are close to those obtained from experiments in upright cylinders for the same  $Ra$ ;  $\omega = 0.09$  s<sup>-1</sup> and  $D\dot{\phi} = 3 \times 10^{-5}$  s<sup>-3</sup> (Brown & Ahlers 2008a). Thus, the model is approximately quantitatively self-consistent when applied to different geometries.

The experimentally measured oscillation period is also shown in figure 23 for comparison to the numerical simulations. While the numerical solution of the model accurately predicts the existence of both the SDS and LDS oscillation states with the correct scale for the period of the switching oscillation, there are a couple of discrepancies. One discrepancy is that the observed oscillation period in the SDS state for  $\Gamma = 0.82$  precisely matches the turnover time, in contrast with the plotted prediction which is close to but differs from the turnover time. This suggests that the oscillation is coupled to the LSC turnover, similar to the twisting or sloshing oscillations in upright cylinders (Brown & Ahlers 2009). The prediction plotted corresponds to the resonant frequency, which should correspond to the observed frequency when the system is driven by white noise. Since the turnover of the LSC can provide a driving frequency, which is close to the resonant period, then it can easily drive oscillations coupled to the turnover period.

A second discrepancy between experiment and theory in figure 23 appears due to the fact that the model is nearly symmetric around aspect ratio 1, since the horizontal cross-sections having the aspect ratios  $\Gamma$  and  $\Gamma^{-1}$  are nearly equivalent as a shift in  $\Gamma$  by  $\sqrt{2}$  transforms from one to the other (there is a slight asymmetry due to the aspect ratio dependence of  $D/D_m$ ). As a result, the transition between the SDS and LDS states is predicted to occur at aspect ratio  $\Gamma = 1$  when the potential barriers on all sides are equal. However, the experimentally observed transition between the SDS and LDS states is at  $\Gamma = 0.82$ , close to the point where the heater aspect ratio is 1, as explained in §3.4. In addition, the measured period is not symmetric around  $\Gamma = 0.82$ . These asymmetries between large and small aspect ratios must be due to the difference that is not included in the model; namely the vertical variation of the boundaries, including the curvature of the sidewall and heater. This suggests that the Brown–Ahlers model for the LSC pathlength could be improved by taking into account the heater shape in addition to the sidewall shape. We have not performed such an adjustment here because it would only produce minor quantitative changes, and not affect qualitative behaviour. Further study is needed to more generally determine how the LSC forcing and pathlength depend on the combination of heater shape and sidewall with a variable horizontal cross-section.

It is interesting to note that in the LDS phase, the observed period of oscillations follows (4.11), which is of Arrhenius–Kramers type (Arrhenius 1889; Kramers 1940; Hanggi, Talkner & Borkovec 1990). However, the Arrhenius–Kramers model is intended to apply to a stochastic switching across a potential barrier with randomly distributed switching times (like a Poisson process), whereas the observed oscillations in the LDS phase have a regular period. The Brown–Ahlers model allows for both regular periodic switching between corners with a period close to  $\tau$ , for higher kinetic energies (large  $D \cdot \tau / U$ ) as observed in the SDS phase, and stochastic switching with the mean period following the Arrhenius–Kramers prediction at lower kinetic energies. In the periodic case, the potential barrier is predicted to have relatively little effect on the oscillation period. Oddly, the observed LDS phase seems to have features of both model regimes. Again, since we developed the Brown–Ahlers model accounting only for the horizontal cross-section at the mid-height of the cell (i.e. ignoring the wall curvature), the models for the SDS and LDS phases are equivalent with a shift in  $\Gamma$  by  $\sqrt{2}$ . Thus, the difference in the oscillation period between the SDS and LDS phases must be due to some effect of the curved sidewall.

#### 4.6. Periodic rocking

The PR phase is notable because it is only found for  $\Gamma > 1$ , so it must be due to some aspect of the curved sidewall. The PR mode is also reminiscent of various oscillation

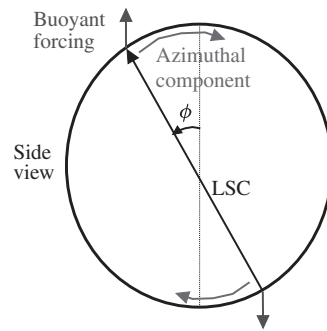


FIGURE 24. Side view of the cell illustrating the oscillation in the PR mode. The restoring force for this mode may come from the azimuthal component of a buoyant forcing on the LSC near the curved wall for  $\beta > 0.82$ .

modes observed in upright cylinders. The coupled twisting and sloshing oscillation mode of the LSC observed in the upright cylinders was explained as due to a restoring force provided by the curved sidewalls when the LSC is displaced from a central path (Brown & Ahlers 2009); this force has the same origin as the pressure from the sidewall responsible for the potential  $U_h(\cdot)$ . A similar situation occurs in an upright cylinder tilted relative to gravity, in which the flow moves upslope along the hot plate and downslope along the cold plate (Brown & Ahlers 2008b). This leads to a restoring buoyant force when the LSC was slightly displaced from the preferred path, producing an in-phase oscillation around the cylinder axis and centred on the preferred path.

In the horizontal cylinder, a similar buoyant forcing can act on the LSC plane when it is slightly tilted at an angle  $\phi$  relative to the central vertical plane which extends along the cylinder axis for  $\beta > 1$ , as shown in figure 24. Modelling the LSC as a rigid rotor, a vector analysis of the buoyancy forcing gives a component of the forcing that pushes the LSC toward  $\phi = 0$ . This restoring force can lead to an azimuthal oscillation of the LSC plane around its preferred vertical alignment at  $\phi = 0$ . These features are exactly those inferred from the observed in the PR mode. This mode cannot occur for  $\beta < 0.82$  in the experimental geometry, since there is no restoring force when the LSC plane is slightly displaced from parallel to the flat end caps. This explains the observation that the PR phase is not found for  $\beta < 0.82$ .

Evaluating the vector balance of the buoyancy forces for the circular cell geometry gives a contribution to the angular acceleration of

$$\ddot{\theta}_{PR} = (2 \beta g / D) \sin \theta - 318 Re^{3/2} \theta^2 / D^4 \quad (4.13)$$

for small angles  $\theta$ , where  $\theta$  is the horizontal temperature difference due to the LSC, and using the approximate scalings for the Reynolds number  $Re(\cdot)$  from Brown & Ahlers (2008a). This results in a resonant frequency  $\omega_{PR} = (\ddot{\theta}_{PR})^{1/2} = 18 Re^{3/4} / D^2$ . If we define  $Re = D^2 / \nu$ , the resonant frequency  $\omega_{PR}$  is of the order of the LSC turnover rate  $1/\tau$  for  $Re$  in the range of the experiments, similar to the observed PR frequency. However, the observed scaling of the period  $t_R$  with  $Re$  and  $\beta$  in the PR phase are not reproduced by this simple model.

## 5. Summary

We have carried out a comprehensive study of the effects of cell geometry on the LSC of turbulent Rayleigh–Bénard convection in a horizontal cylindrical cell filled

with water. An LSC with its rotation plane aligned along the longest path of the cell, namely the diagonal of the cylinder, is observed in the horizontal cells with varying aspect ratios in the range of  $0.16 < \Gamma < 1.69$ . The dynamics of LSC are found to be different from those in the upright cylinders and they have shown strong dependence on the aspect ratio  $\Gamma$ . Four different flow modes are identified with increasing  $\Gamma$ : (i) 2DR for  $0.16 < \Gamma < 0.82$ ; (ii) SDS for  $0.16 < \Gamma < 0.82$ ; (iii) LDS for  $0.82 < \Gamma < 1.69$ ; and (iv) PR for  $1.30 < \Gamma < 1.69$ . The periodic oscillations of the LSC in the SDS, LDS and PR states are new flow modes, which have not been observed in upright cylinders.

In the 2DR phase ( $0.16 < \Gamma < 0.82$ ), the flow is quasi-2D and is confined in the circular plane of the cell. A well-defined oscillation is observed in the power spectrum of local temperature and velocity signals as well as from the flow visualization measurements. From these measurements, we conclude that the coherent oscillations are produced by periodic emission of thermal plumes from the upper and lower thermal boundary layers, which gives rise to a pulsed LSC in the circulation plane of the cell. The oscillations in the thin cell are explained by a new solution of Villermaux's model (Villermaux 1995; Song *et al.* 2011), which considered the interaction between the top and bottom thermal boundary layers as two coupled oscillators.

In the SDS phase ( $0.16 < \Gamma < 0.82$ ), the rotation plane of the LSC switches periodically between the two diagonals of the cell, spanning across the curved sidewall. It is found that the switching period  $t_0$  is approximately equal to the LSC turnover time  $\tau$ .

In the LDS phase ( $0.82 < \Gamma < 1.69$ ), the periodic switching of the LSC orientation remains along the two longest diagonals of the cell but the switching in this case spans across the flat end wall of the cell. The switching period  $t_0$  shows a sharp increase near the transition aspect ratio  $\Gamma_c = 0.82$  and decays exponentially with increasing  $\Gamma$ . The longest switching period  $t_0$  obtained near  $\Gamma_c$  is 5.3 times larger than  $\tau$ .

In the PR phase ( $1.30 < \Gamma < 1.69$ ), the flow becomes quasi-2D again with the bulk fluid as a whole rotating around the central axis of the horizontal cylinder with periodic reversals. The rocking period is found to increase linearly with  $\Gamma$ . The quasi-2D PR phase coexists with the LDS phase. The two flow modes compete and the state of the LSC randomly switches from one to the other.

The measured p.d.f.  $P(\theta)$  of the angular position  $\theta(t)$  of the LSC orientation peaks at the two diagonal positions, and its shape is adequately described by a model proposed by Brown & Ahlers (2008*a,b*). This model consists of stochastic ordinary differential equations in which turbulent fluctuations drive motion a cell-geometry-dependent potential  $U_h(\theta)$ , which controls the dynamics of the LSC orientation  $\theta(t)$ . The calculated  $U_h(\theta)$  has a double-well shape and the barrier height  $U(\theta)$  between the two potential wells decreases with increasing  $\Gamma$ , with potential minima near the cell corners. These features of the model agree well with the experimental results.

We introduced a new correction to the Brown–Ahlers model for the finite width of the LSC, which effectively smooths the potential to better fit the measured  $P(\theta)$ . This correction leads to closed-form solutions for oscillations around a potential minimum driven by stochastic fluctuations, matching the newly observed wiggling mode. This correction also causes the potential to transition from two wells to one well as  $\Gamma$  is decreased below  $\Gamma_c = 0.16$ , corresponding to the observed 2DR phase with a single-peaked  $P(\theta)$ .

The Brown–Ahlers model predicts the periodic switching between the nearest corners in the SDS and LDS states as oscillations in the wider double-well potential, where the stochastic kinetic energy of the LSC is large enough to regularly cross

over the potential barrier. The oscillation in the PR phase may be possible due to a restoring force from buoyancy with a component along the curved sidewall when the LSC plane becomes tilted relative to the vertical plane which extends along the cylinder axis for  $\gamma > 1$ , analogous to the restoring force responsible for oscillations in tilted upright cylinders (Brown & Ahlers 2008b).

In the LDS state, the normalized switching period  $t_0/\tau$  is found to be related to the barrier height  $U_m(\gamma)$  via (4.11), which is of Arrhenius–Kramers type (Arrhenius 1889; Kramers 1940; Hanggi *et al.* 1990) for random switching between potential wells. This is in contrast to the predicted and observed periodic switching in this regime, in which case the switching period is predicted to have a much weaker dependence on the barrier height. We applied the Brown–Ahlers model without taking into consideration of vertical variation in the cell shape, so that the SDS and LDS phases are equivalent to each other with a rotation in  $\gamma$  by  $\pi/2$ . Since the model can accurately predict the oscillation period in the SDS state, we conclude that the discrepancy with the periods in the LDS and PR states has something to do with the fact that the cell shape is non-uniform in height, i.e. with the curved sidewall or the heater geometry. A further understanding of the contribution of vertical variations in the geometry to the LSC dynamics remains open for future studies.

The new features found in the horizontal cylinders and their dependence on the aspect ratio and shape of the convection cell provide important insights toward our understanding of many large-scale convective flows occurring in nature and industry. We find the Brown–Ahlers approach of using a geometry-dependent potential  $U_h(\gamma)$  captures the essential features of the LSC dynamics in the horizontal cylinder. This success suggests promise for this approach to be able to predict single-roll LSC dynamics in arbitrary geometries with a geometry-dependent potential. We propose that multiple-roll flows found in experiments and natural flows with more extreme aspect ratios may require an additional equation for the dynamics of the orientation for each roll with interaction terms between neighbouring rolls, but such an extension to multiple-roll flows remains an open problem for future studies.

### Acknowledgements

We have benefited from illuminating discussions with L. Kadanoff and D. Lohse. This work was supported in part by the Hong Kong Research Grants Council under grant number HKUST-604310 (P.T.) and the United States National Science Foundation CAREER program under grant number CBET-1255541 (E.B.).

### REFERENCES

- AHLERS, G., FUNFSCHILLING, D. & BODENSCHATZ, E. 2009a Transitions in heat transport by turbulent convection at Rayleigh numbers up to  $10^{15}$ . *New J. Phys.* **11**, 123001.
- AHLERS, G., GROSSMANN, S. & LOHSE, D. 2009b Heat transfer and large-scale dynamics in turbulent Rayleigh–Bénard convection. *Rev. Mod. Phys.* **81** (2), 503–537.
- ARRHENIUS, S. 1889 On the reaction rate of the inversion of non-refined sugar upon souring. *Z. Phys. Chem.* **4**, 226–248.
- BELMONTE, A., TILGNER, A. & LIBCHABER, A. 1993 Boundary layer length scales in thermal turbulence. *Phys. Rev. Lett.* **70**, 4067–4070.
- BRENT, A. D., VOLLER, V. R. & REID, K. J. 1988 Enthalpy-porosity technique for modelling convection-diffusion phase change application to the melting of a pure metal. *Numer. Heat Transfer* **13**, 297–318.

- BROWN, E. & AHLERS, G. 2006 Rotations and cessations of the large-scale circulation in turbulent Rayleigh–Bénard convection. *J. Fluid Mech.* **568**, 351–386.
- BROWN, E. & AHLERS, G. 2007 Large-scale circulation model for turbulent Rayleigh–Bénard convection. *Phys. Rev. Lett.* **98** (13), 134501.
- BROWN, E. & AHLERS, G. 2008a Azimuthal asymmetries of the large-scale circulation in turbulent Rayleigh–Bénard convection. *Phys. Fluids* **20**, 105105.
- BROWN, E. & AHLERS, G. 2008b A model of diffusion in a potential well for the dynamics of the large-scale circulation in turbulent Rayleigh–Bénard convection. *Phys. Fluids* **20**, 075101.
- BROWN, E. & AHLERS, G. 2009 The origin of oscillations of the large-scale circulation of turbulent Rayleigh–Bénard convection. *J. Fluid Mech.* **638**, 383–400.
- CASTAING, B., GUNARATNE, G., HESLOT, F., LIBCHABER, A., KADANOFF, L., THOMAE, S., WU, X., ZALESKI, S. & ZANETTI, G. 1989 Scaling of hard thermal turbulence in Rayleigh–Bénard convection. *J. Fluid Mech.* **204**, 1–30.
- CATTANEO, F., EMONET, T. & WEISS, N. 2003 On the interaction between convection and magnetic fields. *Astrophys. J.* **588**, 1183–1198.
- CHAVANNE, X., CHILLÀ, F., CHABAUD, B., CASTAING, B. & HÉBRAL, B. 2001 Turbulent Rayleigh–Bénard convection in gaseous and liquid He. *Phys. Fluids* **13**, 1300.
- CHILLÀ, F. & SCHUMACHER, J. 2012 New perspectives in turbulent Rayleigh–Bénard convection. *Eur. Phys. J. E* **35**, 58.
- CIONI, S., CILIBERTO, S. & SOMMERIA, J. 1997 Strongly turbulent Rayleigh–Bénard convection in mercury: comparison with results at moderate Prandtl number. *J. Fluid Mech.* **335**, 111–140.
- DAYA, Z. A. & ECKE, R. E. 2001 Does turbulent convection feel the shape of the container?. *Phys. Rev. Lett.* **87** (18), 184501.
- DU, Y.-B. & TONG, P. 2000 Turbulent thermal convection in a cell with ordered rough boundaries. *J. Fluid Mech.* **407**, 57–84.
- DU, Y.-B. & TONG, P. 2001 Temperature fluctuations in a convection cell with rough upper and lower surfaces. *Phys. Rev. E* **63**, 046303.
- DYKMAN, M. I., MANNELLA, R., MCCLINTOCK, P. V. E., MOSS, F. & SOSKIN, S. M. 1988 Spectral density fluctuations of a double-well dung oscillator driven by white noise. *Phys. Rev. A* **37**, 1303.
- FUNFSCHILLING, D. & AHLERS, G. 2004 Plume motion and large-scale circulation in a cylindrical Rayleigh–Bénard cell. *Phys. Rev. Lett.* **92** (19), 194502.
- FUNFSCHILLING, D., BROWN, E., NIKOLAENKO, A. & AHLERS, G. 2005 Heat transport by turbulent Rayleigh–Bénard convection in cylindrical samples with aspect ratio one and larger. *J. Fluid Mech.* **536**, 145–154.
- GITTERMAN, M. 2005 *The Noisy Oscillator, The First Hundred Years, From Einstein Until Now*. World Scientific.
- HANGGI, P., TALKNER, P. & BORKOVEC, M. 1990 Reaction rate theory: fifty years after Kramers. *Rev. Mod. Phys.* **62**, 251–342.
- HARTMANN, D. L., MOY, L. A. & FU, Q. 2001 Tropical convection and the energy balance at the top of the atmosphere. *J. Clim.* **14**, 4495–4511.
- HE, X., FUNFSCHILLING, D., NOBACH, H., BODENSCHATZ, E. & AHLERS, G. 2012 Transition to the ultimate state of turbulent Rayleigh–Bénard convection. *Phys. Rev. Lett.* **108**, 024502.
- HUNT, G. R. & LINDEN, P. F. 1999 The fluid mechanics of natural ventilation displacement ventilation by buoyancy-driven flows assisted by wind. *Build. Environ.* **34**, 707–720.
- KADANOFF, L. P. 2001 Turbulent heat flow: structures and scaling. *Phys. Today* **54**, 34–39.
- KRAMERS, H. A. 1940 Brownian motion in a field of force and the diffusion model of chemical reaction. *Physica* **7**, 284–304.
- LOHSE, D. & XIA, K.-Q. 2010 Small-scale properties of turbulent Rayleigh–Bénard convection. *Annu. Rev. Fluid Mech.* **42**, 335–364.
- MARSHALL, J. & SCHOTT, F. 1999 Open-ocean convection: observations, theory, and models. *Rev. Geophys.* **37**, 1–64.
- MCKENZIE, D. P., ROBERTS, J. M. & WEISS, N. O. 1974 Convection in the Earth's mantle: towards a numerical simulation. *J. Fluid Mech.* **62**, 465–538.

- NIEMELA, J. J., SKRBEK, L., SREENIVASAN, K. R. & DONNELLY, R. J. 2000 Turbulent convection at very high Rayleigh numbers. *Nature* **404**, 837–840.
- NIEMELA, J. J. & SREENIVASAN, K. R. 2003 Rayleigh-number evolution of large-scale coherent motion in turbulent convection. *Eur. Phys. Lett.* **62**, 829.
- DU PUIITS, R., RESAGK, C. & THESS, A. 2007 Breakdown of wind in turbulent thermal convection. *Phys. Rev. E* **75**, 016302.
- DU PUIITS, R., RESAGK, C. & THESS, A. 2009 Structure of viscous boundary layers in turbulent Rayleigh–Bénard convection. *Phys. Rev. E* **63**, 046303.
- QIU, X.-L., SHANG, X.-D., TONG, P. & XIA, K.-Q. 2004 Velocity oscillations in turbulent Rayleigh–Bénard convection. *Phys. Fluids* **16**, 412–423.
- QIU, X.-L. & TONG, P. 2001a Large-scale velocity structures in turbulent thermal convection. *Phys. Rev. E* **64** (3), 036304.
- QIU, X.-L. & TONG, P. 2001b Onset of coherent oscillations in turbulent Rayleigh–Bénard convection. *Phys. Rev. Lett.* **87** (9), 094501.
- QIU, X.-L. & TONG, P. 2002 Temperature oscillations in turbulent Rayleigh–Bénard convection. *Phys. Rev. E* **66** (2), 026308.
- RESAGK, C., DU PUIITS, R., THESS, A., DOLZHANSKY, F. V., GROSSMANN, S., ARAUJO, F. F. & LOHSE, D. 2006 Oscillations of the large-scale wind in turbulent thermal convection. *Phys. Fluids* **18**, 095105.
- SETTLES, G. S. 2001 *Schlieren and Shadowgraph Techniques: Visualizing Phenomena in Transparent Media*. Springer.
- SONG, H. Effects of geometry on turbulent Rayleigh–Bénard convection. PhD thesis, Hong Kong University of Science and Technology.
- SONG, H. & TONG, P. 2010 Scaling laws in turbulent Rayleigh–Bénard convection under different geometry. *Eur. Phys. Lett.* **90**, 44001.
- SONG, H., VILLERMAUX, E. & TONG, P. 2011 Coherent oscillations of turbulent Rayleigh–Bénard convection in a thin vertical disk. *Phys. Rev. Lett.* **106**, 184504.
- SUN, C., CHEUNG, Y. H. & XIA, K. Q. 2008 Experimental studies of the viscous boundary layer properties in turbulent Rayleigh–Bénard convection. *J. Fluid Mech.* **605**, 79–113.
- SUN, C., REN, L. Y., SONG, H. & XIA, K.-Q. 2005a Heat transport by turbulent Rayleigh–Bénard convection in 1m diameter cylindrical cells of widely varying aspect ratio. *J. Fluid Mech.* **542**, 165–174.
- SUN, C., XIA, K.-Q. & TONG, P. 2005b Three-dimensional flow structures and dynamics of turbulent thermal convection in a cylindrical cell. *Phys. Rev. E* **72** (2), 026302.
- SUN, C., ZHOU, Q. & XIA, K.-Q. 2006 Cascades of velocity and temperature fluctuations in buoyancy-driven thermal turbulence. *Phys. Rev. Lett.* **97**, 144504.
- URBAN, P., MUSILOVÁ, V. & SKRBEK, L. 2011 Efficiency of heat transfer in turbulent Rayleigh–Bénard convection. *Phys. Rev. Lett.* **107**, 014302.
- VILLERMAUX, E. 1995 Memory-induced low frequency oscillations in closed convection boxes. *Phys. Rev. Lett.* **75** (25), 4618–4621.
- XI, H.-D. & XIA, K.-Q. 2007 Cessations and reversals of the large-scale circulation in turbulent thermal convection. *Phys. Rev. E* **75** (6), 066307.
- XI, H.-D., ZHOU, Q. & XIA, K.-Q. 2006 Azimuthal motion of the mean wind in turbulent thermal convection. *Phys. Rev. E* **73** (5), 056312.
- XI, H.-D., ZHOU, S.-Q., ZHOU, Q., CHAN, T.-S. & XIA, K.-Q. 2009 Origin of the temperature oscillation in turbulent thermal convection. *Phys. Rev. Lett.* **102** (4), 044503.
- XIN, Y. B., XIA, K. Q. & TONG, P. 1996 Measured velocity boundary layers in turbulent convection. *Phys. Rev. Lett.* **77**, 1266–1269.
- ZHOU, S. Q., SUN, C. & XIA, K.-Q. 2007 Measured oscillations of the velocity and temperature fields in turbulent Rayleigh–Bénard convection in a rectangular cell. *Phys. Rev. E* **76**, 036301.
- ZHOU, Q., XI, H. D., ZHOU, S. Q., SUN, C. & XIA, K.-Q. 2009 Oscillations of the large-scale circulation in turbulent Rayleigh–Bénard convection. *J. Fluid Mech.* **630**, 367–390.
- ZOCCHI, G., MOSES, E. & LIBCHABER, A. 1990 Coherent structures in turbulent convection, an experimental study. *Physica A* **166**, 387–407.